Dissertation
submitted to the
Combined Faculty of Natural Sciences and Mathematics
of the Ruperto Carola University Heidelberg, Germany
for the degree of
Doctor of Natural Sciences

Presented by

M.Sc Sourabh Bhide

born in Pune, India

Oral examination: January 22nd 2019

Co-ordination of cell shape changes during ventral furrow formation in *Drosophila* embryo

Referees: Dr. Takashi Hiiragi

Jun-Prof. Dr. Steffen Lemke

Abstract

The formation of the ventral furrow in the *Drosophila* embryo has served as one of the major paradigms for how large-scale morphogenetic events are initiated, controlled and mediated by cellular behavior. The furrow is formed by the inward folding of the mesoderm epithelium on the ventral side of the early embryo. While it is well established that the onset of gastrulation is initiated by the apical constriction of the central mesoderm cells (CM), a subpopulation about 8-10 rows wide, it has recently become clear that furrow internalization can only be completed with the cooperation of the lateral mesodermal (LM) cells, a subpopulation about 3-4 rows wide on each side of the mesoderm that, instead of constricting, expand their apical areas at the same time. In this thesis we have developed a method to reconstruct 3D cell-volumes in the entire embryo to study the coordination of cells shape changes during ventral furrow formation. We find that the cell shape changes in LM cells are passive and depend on the forces generated during apical constriction in the CM cells. A *twist* induced gradient of molecular cascade leading to apical MyosinII recruitment in the mesoderm results into a 'tug-of-war' between the adjacent cells. Due to high amount of apical MyosinII recruitment, the CM cells constrict stronger and causes the LM cells to expand apically.

Zusammenfassung

Die Bildung der ventralen Furche im Drosophila Embryo ist eines der an den besten erforschten Paradigmen dafür wie großflächige morphogenetische Ereignisse,durch das Verhalten einzelner Zellen oder Zellgruppen, initiiert und gesteuert werden. Die Furche entsteht durch das Einfalten des Mesoderm-Epithels auf der ventralen Seite des Embryos. Durch das Zusammenziehen des zentralen Mesoderms, (ZM) das 8-10 Zellreihen umfasst, wir die Gastrulation eingeleitet. Sie kann jedoch nur erfolgreich ablaufen, wenn sich gleichzeitig das laterale Mesoderm (LM), eine Untergruppe von 3-4 Zellreihen auf beiden Seiten des Mesoderms, apikal streckt. Mit dieser Arbeit haben wir eine 3D Rekonstruktionsmethode entwickelt die es uns ermöglicht die Zellvolumina im kompletten Embryo zu verfolgen. Auf diese Weise lassen sich die Veränderungen der Zellformen wären der Entstehung der ventralen Furche untersuchen. Wir haben herausgefunden, dass die Veränderung der Zell form im LM passiv ablaufen und abhängig von der Kraft sind mit der sich das ZM zusammenzieht. Durch *twist* entsteht ein Gradient apikaler Rekrutierung von MyosinII entlang des Mesoderms, was zu einem Effekt des Tauziehens zwischen benachbarten Zellen führt. Die stärkere Rekrutierung von MyosinII in den ZM Zellen hat zur Folge, dass sich diese stärker zusammenziehen als die LM Zellen, welche sich infolgedessen apikal ausdehnen.

Contents

List of figures

List of Tables

List of Abbreviations

2D	Two dimensional
3D	Three dimensional
AJ	Adherens junctions
AP	Anterior-posterior
ATP	Adenosine triphosphate
CM	Central mesodermal
DNA	Deoxyribose nucleotide acid
dsRNA	Double-stranded RNA
DV	Dorsal-ventral
eGFP	Enhanced green flourescent protein
GAP	GTPase activating protein
GDI	Guanine nucleotide dissociation inhibitor
GDP	Guanine diphosphate
GEF	Guanine nucleotide exchange factor
GFP	Green flourescent protein
GPCR	G protein coupled receptors
GTP	Guanine triphosphate
LM	Lateral mesodermal
mCherry	Monomeric cherry flourescent protein
ME	Mesectodermal
MRLC	MyosinII regulatory light chain
MuVI-SPIM	Multi view selective plane illumination microscope
NA	Numerical aperture
NC	Nuclear cycle

PSF	Point spread function
RNA	Ribose nucleotide acid
RNAi	RNA interference
shRNA	Small hairpin RNA
SPIM	Selective plane illumination
VFF	Ventral furrow formation

1. Mechanisms of cells shape changes during ventral furrow formation

1.1 Shape changes during gastrulation

Shape changes in the mesoderm

Embryo development in Drosophila begins with 14 cycles of synchronized nuclear divisions without cytokinesis. After 9 cycles of nuclear division, the nuclei migrate to the surface of the embryo and undergo further four cycles of nuclear division. After the 14th nuclear division cycle, plasma membrane starts to grow inwards from the surface and encloses the nuclei. At this stage, the embryo is a uniform monolayered epithelium of about 5000 cells. A stripe of ~ 20 cells covering about 80% of the circumference on the ventral side, fold inwards forming a tube. These invaginated cells form the mesodermal structures like heart and muscles. Mesoderm primordia and the overlying neuro-ectoderm stretch around the posterior of the embryo in a process called germ band extension. The mesoderm invagination followed by the germ band extension are the first large scale morphogenetic events that transform the embryo from a monolayered to a bilayered embryo[1,2].

At the onset of mesoderm invagination, the cells on the ventral side begin to change their shapes; a central population about 8-10 rows-wide start reducing their apical cross-sectional area while two lateral populations, about 2-3 rows-wide on either side of the central population start expanding their apical area. Cells of both the cell population lengthen along the apical-basal direction (Fig 1.1). The nuclei of the central mesodermal (CM) cells which are more sub-apical move basally while the nuclei of the lateral mesodermal (LM) cells continue to remain sub-apical. Consequently, the CM cells shorten along their apical-basal axis, expand basally and are internalised as a tube. The LM cells, keep expanding their apical domain and form the stock of the tube. Both, the CM cells and LM cells then undergo epithelial to mesenchymal

transition and start dividing and differentiating to give rise to mesodermal structures.

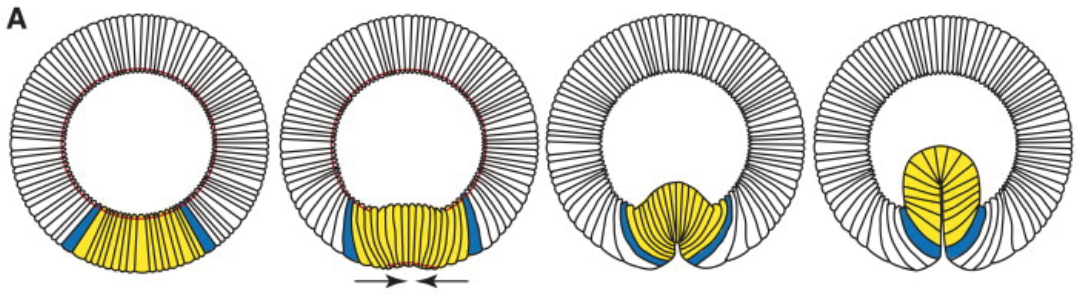

Fig 1.1. Representation of a cross-sectional view of cell shape changes and movements during *Drosophila* gastrulation. Mesodemal cells (yellow) change their shapes and are internalised, while lateral cells (white) move ventrally. Red color represents localisation of active MyosinII and arrows represent apical constriction. (Adapted from Woolner, 2007[3])

Contribution of the neighbouring cells

Shape changes in the prospective mesoderm have been the centre of study for more than two decades. We still do not completely understand how the rest of the embryo responds to the shape changes in the mesoderm. Our current understanding comes from the work of Rauzi and colleagues from the Leptin lab. Using Multi View Selected Plane Illumination Microscopy (MuVi SPIM) to image the entire embryo, they identified 4 subpopulations of cells with distinct behaviour along the dorso-ventral axis: central mesodermal cells, lateral mesodermal cells, ectodermal cells and the dorsal cells. The resultant images of the apical cross-sections were then projected cartographically on a two-dimensional sheet were then fitted on to a cylinder and then processed to give a cartographic display. This allowed them to project the apical area cross-sections of the entire embryos onto a two dimensional sheet (Fig.2 left). These datasets were then used to track cell centroid positions in time and construct a kymograph along a imaginary line, midway between the anterior and posterior end (Fig.2 right). The authors observed that the cell shape changes in the ectoderm can be separated into two distinct phases: 1) Phase

one coincides with the onset of gastrulation and up until 3 minutes after the formation of the ventral furrow, 2) Phase two continues from this point onward until the furrow is invaginated In the first phase, ventral cells constrict apically, and ventrolateral cells stretch towards the ventral midline, during this phase the lateral cells do not move or change their shape. During the second phase, after initial formation of the ventral furrow, cells in the lateral cells "shift ventrally as a compact cohort", and those in the dorsal ectoderm stretch and elongate towards the ventral part of the embryo. The behaviour of the lateral mesodermal cell was omitted from the analysis and the focus was on the contribution of the ectodermal and dorsal cells to mesoderm invagination. Live imaging, laser ablation and cauterisation experiments show that ectoderm does not directly contribute to furrow formation, but its movement contributes in furrow invagination[4]. While we know that the movement of lateral cells is not dependent on furrow formation, the mechanisms underlying this movement are not fully understood. Expansion of the dorsal cells does not seem to directly or indirectly contribute to furrow formation and invagination.

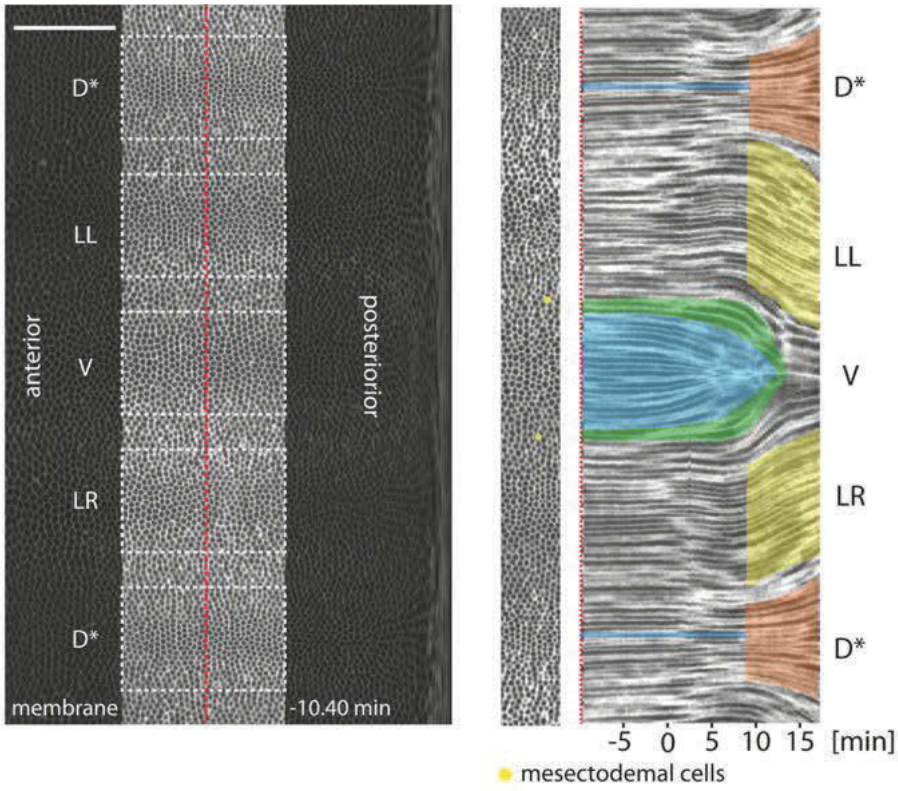

Fig 1.2 Analysis of embryo-wide apical shape changes and movements. **A**. Cartographic projection of the apical surface of the entire embryo before gastrulation. The dorsal cells (D*) are duplicated to emphasize the symmetry in the embryo. **B.** Kymograph along middle of the embryo marked by dotted red line in **A.** Yellow dots represent the mesectoderm cells. The kymograph shows four cell populations based on their cell movements: CM cells (blue), LM (green) cells, lateral ectodermal cells (LR,yellow) and dorsal ectodermal cells (D*,red). (Adapted from Rauzi et al., 2015 [4]**)**

1.2 Molecular pathways involved in mesoderm invagination

Mesoderm invagination has been a convenient model to understand the bridge between developmental patterning, signaling and tissue morphogenesis. As a result, we know a lot about the molecular players involved in the entire process.–Three factors regulate mesoderm invagination (i) developmental patterning; (ii) signalling components and iii) effector molecules. In the following section I would like to describe the functional role of key molecules regulating mesoderm invagination based on their sequence of activation

Dorso-Ventral patterning

In *Drosophila*, the dorso-ventral (DV) polarity is initiated during oogenesis by an asymmetric signal generated by a cross-talk between the germline derived oocyte and the enveloping somatic follicular cells. During maturation of the oocyte the nucleus migrates from the posterior to the anterior margin of the oocyte[5]. The asymmetric positioning of the oocyte nucleus is the first sign of DV polarity. The oocyte produces a dorsalising signal which is received by the immediate neighbouring follicle cells, thus defining DV polarity. The ligand and receptor for this pathway are encoded by the genes *gurken* and *torpedo* respectively (these are homologs of mammalian epidermal growth factor and its recpetor). The *gurken* transcripts upon translation accumulate in the cytoplasm towards the dorsal side of the egg by stage 10. The Gürken protein diffuses to the neighbouring cells forming a gradient of dorsalising signal. Loss of function in *gürken* and *torpedo* results in ventralised embryos.

Gurken- torpedo signalling blocks expression of *pipe.* Ventral cells that fail to activate Torpedo –express *pipe;* Pipe protein has sulfotransferase activity and it modifies the vitelline membrane of the ventral follicular cells. The modification of the vitteline membrane by Pipe is inherited by the embryo

and it results in the recruitment of different proteases to the perivitteline space. The following proteolytic pathway that assigns the dorso-ventral fates to the cells of the embryo is one of the best understood examples of morphogen derived patterning.

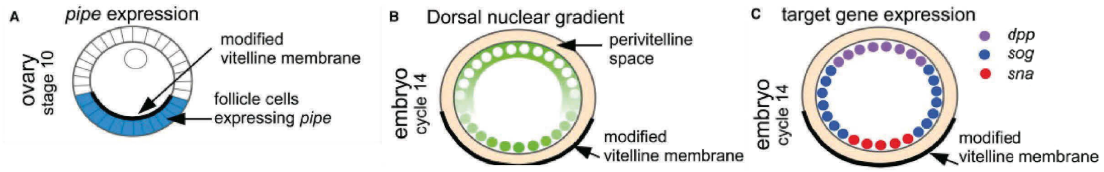

Fig 1.3 Dorso-ventral patterning in Drosophila ovary and embryo A. Schematic cross-sectional representation of stage10 ovary. *Pipe* expressing follicle cells (blue) modify the perivitteline membrane (bold black line) of the egg cell. B. By nuclear cycle 14 in the embryo, the cells adjacent to pipe-modified vitteline membrane localise higher amounts of Dorsal; C. Depending upon the nuclear Dorsal concentration downstream zygotic transcription factor are activated. (Adapted from Haskel-Ittah et al 2012)

The protease cascade in the peri-vitelline space starts with the the activation of Goosecoid (GD). GD ultimately via Snake and Easter cleave and activates Spätzle (spz). Spätzle encodes NGF-like protein that dimerises to bind two monomers of its receptor Toll. Toll is expressed uniformly throughout the embryo but is activated by cleaved Spätzle which is produced only in the ventral cells. However, activated Spätzle diffuses in the perivetteline space and generates a gradient of Toll signalling. The activation of Toll induces an intracellular signalling pathway that disrupts the complex between Dorsal and its antagonist Cactus, leading to the nuclear localisation of Dorsal. The disruption of this complex occurs by degradation of Cactus by Toll activation via two proteins Pelle and Tube. Once Dorsal localises inside the nucleus, it regulates gene expression of many downstream targets. The graded activation of the receptor Toll and downstream signalling determines different cell fates along the dorso-ventral axis. The differential amount of nuclear dorsal divides the embryo in ventral mesoderm, lateral neurectoderm and dorsal ectoderm by activating and repressing different sets of zygotic genes.

Differentiation of the mesoderm

Two Dorsal targets, *snail*-a transcriptional repressor and *twist*- an activator determine the mesodermal fate in *Drosophila*[6,7]*. While* Twist is a helix-loop-helix protein, Snail is zinc-finger protein. Embryos mutant for these genes do not form a mesoderm, although they form lateral and dorsal structures [8,9].

The expression of *snail* and *twist* is detectable by 12th nuclear division cycle (nc), although it might start even before that. After the 14t^{h} nc, expression of *snail* is restricted within band of cells boundary of which is specified by-*singleminded (sim)* expressing cells [10]. *Twist* expression however extends beyond the mesectoderm boundary and is graded with highest expression in the central cells [11,12]. While Dorsal initiates *snail* expression, Twist is required for sustained expression of *snail* throughout mesoderm invagination. *twist* expression defines the domain of mesoderm specification and within this domain it activates and maintains the expression of mesoderm-specific genes, including itself and *snail* . Both, the activation of mesoderm specific genes by Twist and repression of ectodermal genes by Snail, is required for specification and invagination of mesoderm.

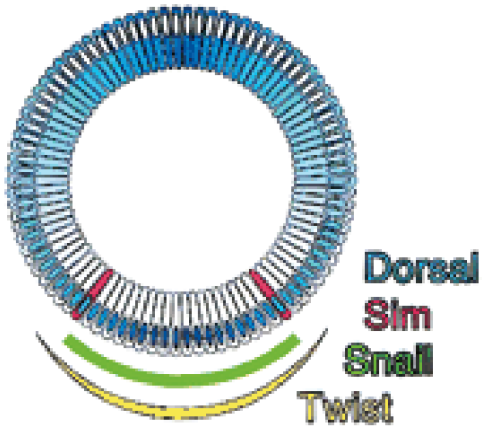

Fig 1.4 Schematic showing expression domains of key mesodermal determinants: Snail and Twist. High amount of nuclear dorsal induces expression of *twist* in a graded manner and uniform *snail* expression bound by a single row of cells expressing *singleminded* (*sim*). (Adapted from Morel V and Schweisguth F 2000 [13]).

Signalling components

Two Twist targets proteins: *folded gastrulation* (*fog*) and *transcript 48* (*t48*) trigger shape changes in mesoderm. While Fog is a secreted ligand, T48 is an apical transmembrane protein. Fog activates at least two known G-protein coupled receptors (GPCRs) and activates Rho GTPase 1 (Rho1) in parallel with signal from t48. Embryos mutant for either fog or t48 show a kinetic delay furrow formation. However, when both fog and t48 are mutated there is complete failure in furrow formation and invagination, suggesting their complementary roles in mesoderm invagination[14]

fog/GPCR signalling

Much of what we know about *fog* comes from looking at apical surfaces of the cells during gastrulation stage. Right before cells in the mesoderm begin to change their shape, their apical surfaces flatten out. Embryos mutant for fog fail to undergo apical flattening and show uncoordinated apical constriction[15] .Similar effects are seen in the invagination of the endoderm occurring at the dorsal-posterior side of the embryo (posterior midgut formation). The cells that form the posterior midgut maintain curved spical surfaces fail to invaginate. Ectopic expression of fog specifically in the posterior midgut of mutant embryos is sufficient to trigger apical flattening and invagination. Also, heat-shock induced fog over expression is known to cause ectopic apical flattening and constrictions in other parts of the embryo[16].

Fog is a 78 kDa secreted protein that is under direct transcriptional control of Twist. The RNA transcripts of fog are detectable in ventral most cells 25 min after the onset of the 14th nc. The expression domains slowly widen over the next 15 minutes spreading over the entire mesoderm. However, cells near the lateral boundaries have relatively low amounts of fog expression. In all, there is a temporal gradation of fog expression along the DV axis[17].

Fog functions as a ligand to activate at least 2 known GPCRs Mist and Smog[18-20]. Mist is known to induce cell constriction on binding to Fog in S2 cells. Mist is zygotically expressed and is a direct target of Snail. Mist

transcripts were detected after onset of nc 14 in the mesoderm. Unlike the ligand fog, mist does not show any graded distribution along the DV axis[17]. Smog is maternally deposited and is expressed uniformly throughout the embryo. While a single RNAi knockdown of either *smog* or *mist* causes a slight delay in ventral furrow formation (VFF) a double RNAi knockdown leads to complete failure[20].

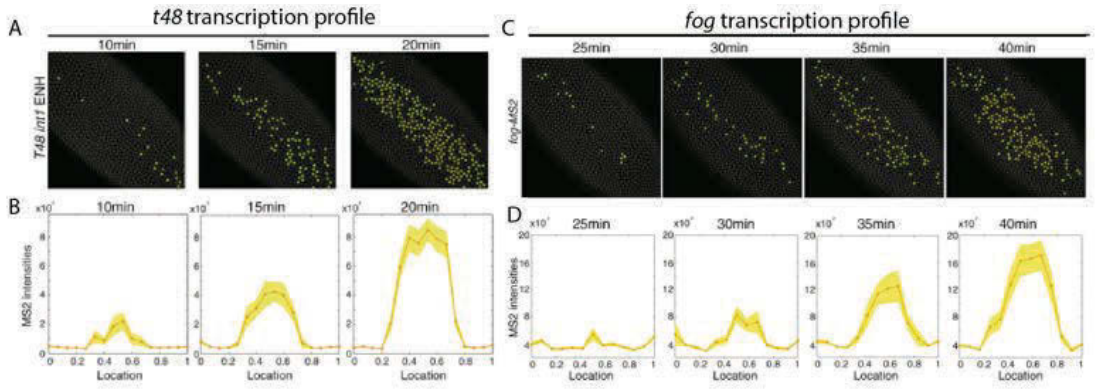

Fig 1.5. Expression profiles of t48 and fog after the 14th nuclear cycle in the mesodermal cells. A and C show falsely colored nuclei expressing *t48* and *fog* respectively. B and D show quantification of nuclear signal of *t48* and *fog* trasncripts, where zero on all the X-axes marks the ventral midline. (Adapted from Lim et. al, 2017 [17])

Activation of the Rho1 pathway in mesoderm is thought to occur via the guanine exchange factor (GEF) functionality of the GPCRs. GPCR complex consists of a transmembrane receptor and the heteromeric G proteins (Gα, Gβ/Gγ subunits). Ligand binding induces a conformational change in GPCR, converting Gα from an inactive-GDP-bound state to an active-GTP-bound state. As a consequence, the Gα dissociates from the Gβ/Gγ subunits. Gα, Gβ/Gγ subunits then facilitate recruitment of two sets of effector molecules and transduce different signalling pathways.

In *Drosophila*, the heteromeric G proteins *Gα12/13, Gβ13F* and *Gγ1* are required for apical constriction during VFF. Apical constriction is abrogated in embryos mutant for either of the G protein subunit[20]. The role of Gβ/Gγ subunits is not clearly understood in respect of apical constriction and

VFF. Gα also known as Concertina (Cta)[21] is required for apical localisation of RhoGTPase nucleotide exchange factor 2 (RhoGEF2) .

t48 signalling

t48 is a direct target of Twist and it codes for a trans membrane protein. Nascent transcripts of t48 are detected as early as nc 14. They start to appear along the ventral midline few minutes after the start of nc 14. The expression increases and covers a 10-14-cell wide domain of the ventral side. The cells expressing the highest amount of t48 transcripts are observed to be close to the ventral midline. Further quantification reveals an existence of a gradient of t48 transcript accumulation by the end of nc 14[17]. Similar observations about the gradient are seen when T48 is endogenously tagged with GFP[12]. This suggest that there exist a gradient of gene expression and protein of apical T48.

A C-terminus consensus sequence of T48 interacts with the PDZ domain of RhoGEF2. This interaction has been shown to facilitate RhoGEF2 recruitment to the plasma membrane in S2 cells. Embryos deficient in T48 display delayed internalisation of the mesoderm. Similar effects are also seen in embryos lacking either *fog* or *cta.* Double mutants for *t48* and *cta* fail to accumulate RhoGEF2 resulting in failure of apical constriction and ventral furrow formation[14]. Thus T48 and Fog/Cta signalling act in parallel to recruit RhoGEF2 to the apical plasma membrane.

Intracellular signalling

Once RhoGEF2 is recruited to the apical membrane, it activates a cascade of downstream effector molecules that organize apical actomyosin meshwork essential for ventral furrow formation. Embryos mutant for *RhoGEF2* fail to initiate furrow formation and thus fail to invaginate[22]. Embryos injected with RNAi against *RhoGEF2* and or over expressing a constitutive form of Concertina fail to accumulate apical MyosinII[20]. This suggests that RhoGEF2 is necessary for apical recruitment and activation of MyosinII. Current models proposes that active Rho1, a small GTPase from

the Ras family, recruits apical MyosinII. The GEF domain of RhoGEF2 activates Rho1 by exchanging GDP with GTP. Recently identified GAP, Cumberland GAP (C-GAP) deactivates RhoA by hydrolyzing the GTP to GDP[23]. Over-expression of a dominant negative form of Rho1 inhibits apical constriction. This phenotype is very similar to RhoGEF2 mutant embryos. Also, ectopic expression of constitutively active form of Rho1 (Rho1-V14) is sufficient to increase contractility in other cells[24]. Once activated, Rho1 can activate several molecules including recruitment of apical MyosinII and organization of the F-Actin meshwork. Rho1 activates Rho kinase (Rok), that further activates the MyosinII regulatory light chain. It also inhibits MyosinII phosphatase which leads to increase MyosinII activity. Rho1 is also implicated in the organization of the apical F-Actin meshwork by activating LIM kinase which is an inhibitor of actin severing protein Cofilin. Small molecular inhibitors that can disrupt Rho1 activation-deactivation cycle are yet to be identified.

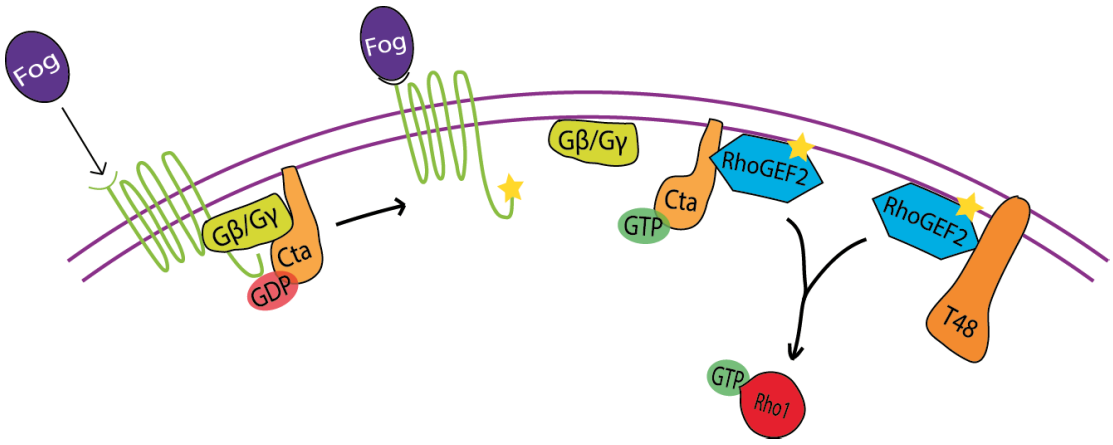

Fig 1.6 A schematic showing parallel activation of RhoGEF2 via Fog and T48. The secreted ligand, Fog binds to its receptors and activates RhoGEF2 via Gα subunit, Cta. Trans-membrane protein T48 recruits and localises RhoGEF2 to plasma membrane

1.3 Apical Constriction

Activation of the RhoGEF2/Rho1 pathway leads to recruitment of apical actomyosin meshwork in the central mesodermal (CM) cells. Experiments to show the molecular mechanisms of apical MyosinII recruitment were done using fixed embryos. Preliminary observations by Adam Martin and colleagues revealed that apical cross-sectional area of individual cells undergoes dynamic changes before apical constriction sets-in. These fluctuations in apical area or 'pulses' correlated with MyosinII coalescence close to the centre of the cells (Fig7 a-b) [25]. Their study showed that MyosinII accumulation in the medial part of the cell strongly correlated with decrease in

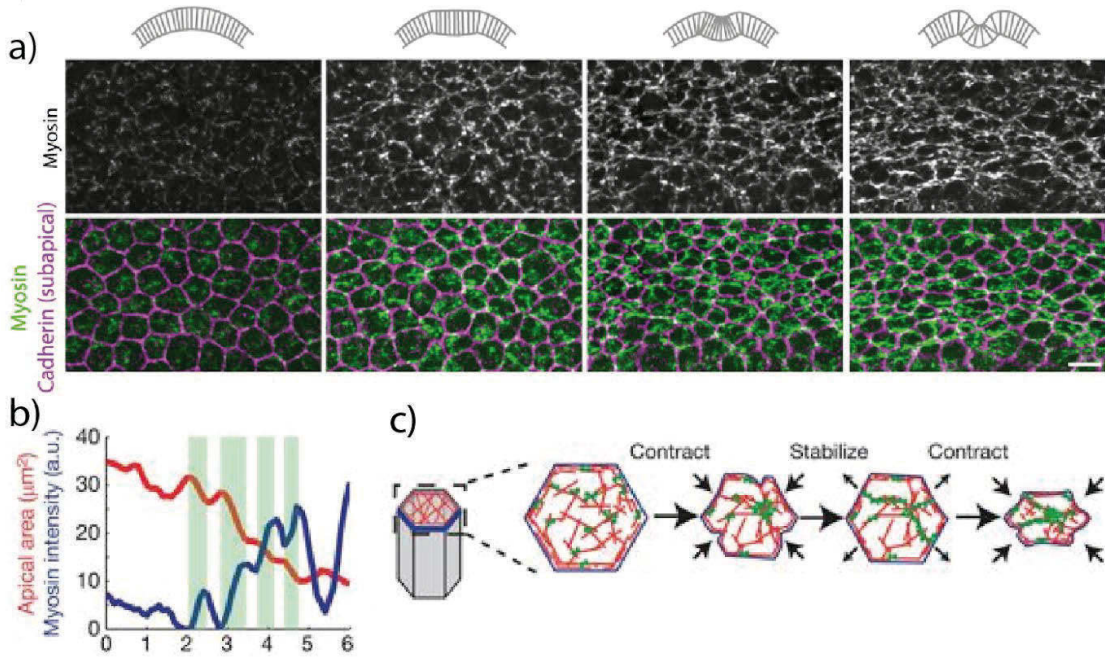

Fig 1.7 Step-wise apical constriction of central mesodermal cells during ventral furrow formation. A. Accumulation of apical MyosinII (grayscale and green) and outline of apical cross-sectional area (magenta) during ventral furrow formation. B. Quantification of apical cross-sectional area (red line) and apico-medial intensity of MyosinII (blue line). Green areas mark time frames where myosinII intensity increases and white gaps mark regions of decrease in apical area. C. Schematic representation of a step-wise apical constriction. (Adapted from Martin et al., 2009 and Martin et al., 2010 [25,26])

the apical area. This effect is further enhanced ~2-3 minutes after the onset of pulses (Fig 1.7 B). The changes in medial MyosinII concentration and apical area are not continuous but occur in step wise manner. The authors propose a ratchet-like model to explain this observation.

In experimental conditions where MyosinII does not accumulate apically, apical constriction fails. Thus there is strong evidence to suggest that contractile forces generated by actomyosin contraction leads to apical constriction. To understand in greater detail about the force generation we need to first understand mechanisms underlying contraction of actomyosin meshwork.

Actomyosin contraction

Actomyosin meshwork are formed by MyosinII motors walking on cross-linked actin filaments. MyosinII molecule has two N-terminal globular domains (head) comprising the heavy chain which contains actin and ATP binding sites and a C-terminal domain (tail) that contains α-helical coiled-coil domains that is required for homodimerization. Upon activation, the inactive-

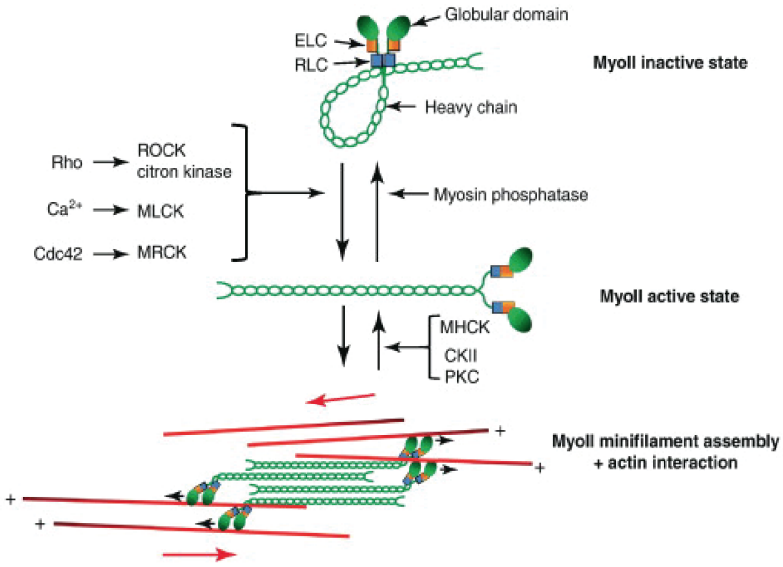

Fig 1.8 Activation of MyosinII. Closed and open conformations of MyosinII motor protein and interaction with actin meshwork. (Adapted from Levayer and Lecuit, 2011[27])

folded MyosinII unfolds and is able to bind to actin filaments and form homomers. The tail domains assemble MyosinII molecules into bipolar filaments with the tails packed in the centre and the head domains at the two ends (Fig 8)[27]

Sliding of MyosinII filaments on antiparallel actin filaments can generate either contractile or expansile forces (Fig 1.9). Contractility of actomyosin meshwork is an integrated effect of these contractile and expansile forces. There have been many theories so far to understand the integration of the aforementioned forces. There are two processes central to the contractile actomyosin meshwork viz. buckling of actin filaments and end dwelling of motor filaments[28].

Since actin filaments are semi-flexible, they readily buckle when subjected to compressive stress. Thus buckling can compensate for any expansile forces within a larger actomyosin meshwork. Theoretical work done by Belmonte and colleagues suggest that for the buckling to affect contractility of actomyosin meshwork, the actin filaments need to be connected by cross linkers[29]. Thus a combined effect of semi-flexible actin filaments, motors and cross linkers can bias an actomyosin meshwork to contract.

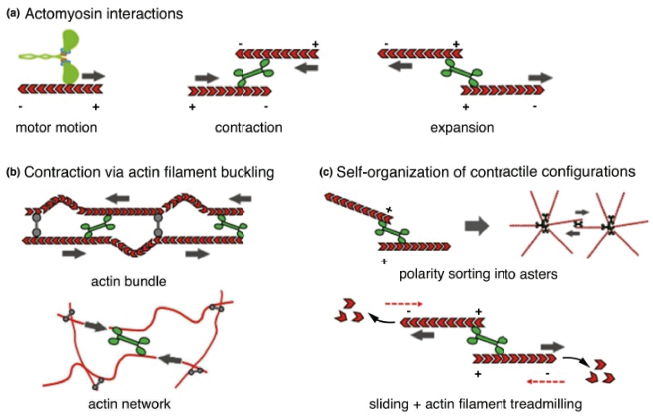

Fig 1.9. Formation of the actomyosin meshworks .A. Schematic of how MyosinII filament generates contraction and expansion of polar actin filments. B-C. Modes of actomyosin meshwork contraction. B. Flexible actin filaments buckle and inhibit net expansion of the meshwork. C. End dwelling mechanism leads to polarity sorting and formation of asters. Rapid turnover of actin can also generate expansile forces. (Adapted from Koenderink and Palusch, 2018[28])

Movement of MyosinII motors is always towards the growing end of actin filaments. When these motors reach the end of the actin filament, they stall before falling off. This stalling behaviour is called 'end dwelling'. The end dwelling property of motor proteins has been suggested to be the primary cause of meshwork contraction for rigid filaments like microtubules. Wollrab V and colleagues have carefully analyzed *in vitro* the actomyosin meshwork contraction by end dwelling mechanism as well as buckling of actin filaments[30] using both invitro and in silico models.

Actomyosin pulses

Actomyosin pulses have been observed in plethora of developmental contexts. They are observed in *Drosophila* embryo during ventral furrow formation, germ band extension, dorsal closure, invagination of the salivary gland, invagination of neuronal precursor cells and many more.

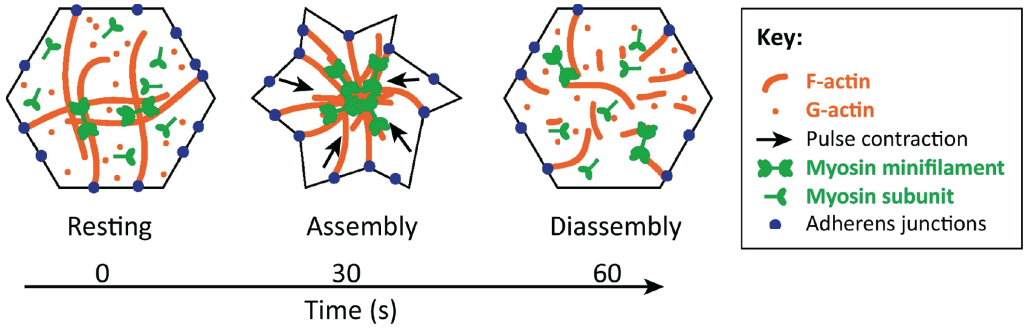

Fig 1.10 A schematic explaining how MyosinII assembles and disassembles accompanied by area fluctuations (Adapted from Caravos et al., 2017 [31]).

A pulse is defined as a cyclical process where at first the MyosinII filaments assemble on the actin filaments which leads to actomyosin meshwork contraction followed by disassembly of MyosinII and actin filaments. We do not yet completely understand how the assembly and disassembly are coordinated. Extensive analysis of ventral furrow formation and germ band extension indicate that Rho/Rok pathway is necessary to activate the MyosinII and initiate the assembly. However, there is no strong evidence that explains how the disassembly occurs. Munjal and colleagues

hypothesized that the assembly and disassembly is self-organised. Their model states that contraction of apical actomyosin generates an advection current in the cytoplasm that mobilises actomyosin-disassembly-promoting factors to the apical side[32]. On delivery of these factors, the meshwork disassembles and can be reassembled by myosin activation.

Actomyosin pulsing during ventral furrow formation

Actomyosin pulses are initiated by activation of the regulatory light chain (RLC) of MyosinII via RoK. It has been observed that perturbing the activity of Rok affects the pulsatility of MyosinII. Pulsatility is nothing but just the measure of frequency and maximum intensity of the MyosinII pulse. The regulators of MyosinII namely Rok, active Rho1 and RhoGEF2 are observed to be pulsing as well. These dynamics are thoight to be due to negative regulation of Rho1 by C-GAP[23] .

According to the model proposed by Mason and colleagues, phosphorylation of MyosinII RLC by Rok via RhoGEF2/Rho1 triggers the actomyosin pulse generation. Additionally, active Rho1 inhibits MyosinII phosphatase and activates Dia, an actin regulator to promote actomyosin contraction. Once actin networks begin to contract, negative regulators like C-GAP and Myosin phosphatase are probably recruited by an advection current. These negative regulators promote disassembly of the contracted actomyosin meshwork. While the advection flow hypothesis needs to be experimentally validated, existing reports suggest that dynamic regulation of Rho1 is the most probable cause for MyosinII pulses.

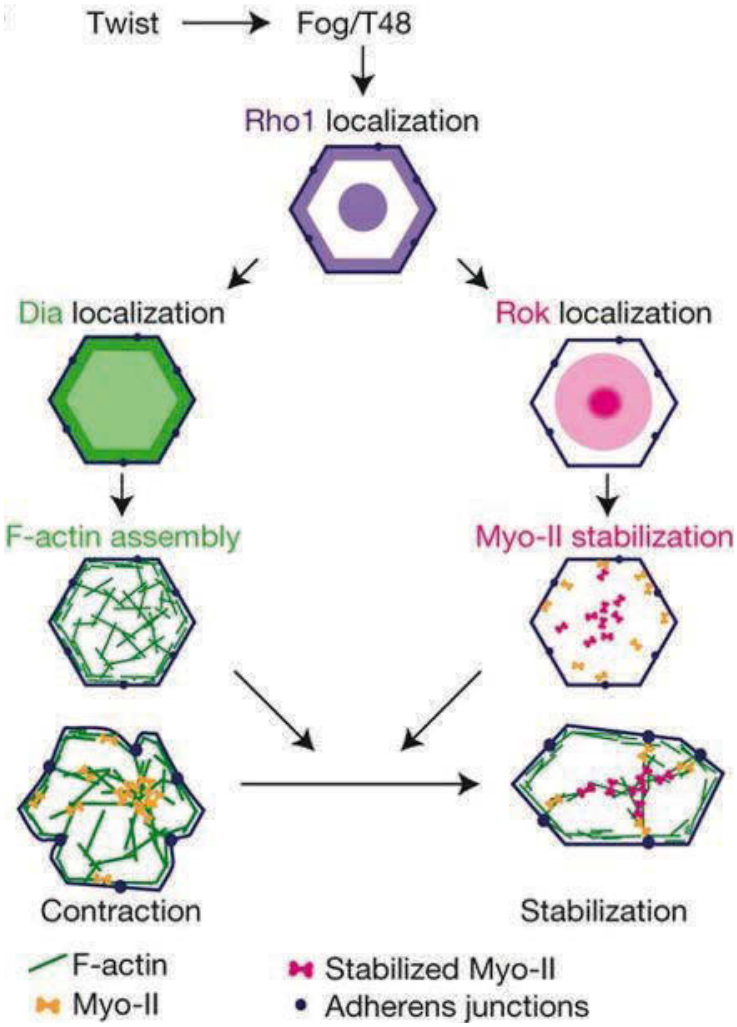

Fig 1.11 A model for Twist-dependent ratcheted contraction. Rho1 organises apical f-actin and activates MyosinII. Rok stabilizes medial MyosinII and results in stabalised contraction. (Adapted from Mason et al., 2016[23])

Martin A. and colleagues observed that apical constriction is a consequence of ratcheted actomyosin contractions. Apical constriction occurs as a result of net contraction after a contraction-relaxation cycle. They observe a Twist dependent increase in active MyosinII levels which correlates with net apical[21]. Viscoelastic behaviour can also be a contributing mechanism for ratcheted behaviour. Viscous dissipation or hysteresis loss can generate a net contraction after a contraction-relaxation cycle. The contribution of hysteresis to irreversible contraction however depends on the time-scales of pulse period [33].

Cellular effects – The volume conservation principle

The forces generated on the apical side are also propagated to the rest of the cell. Gelbart and colleagues analyzed these effects in detail by quantifying the change in volume of the cells using a 2-photon laser. Their observed that while there is reduction in apical cell area and an increase in cell-length the total volume of the cell remains constant. In double mutants of *cta* and *t48* the apical constriction is abolished and there is no cell lengthening while the volume is constant. The authors hypothesise that the cell lengthens as an effect of incompressible cytoplasm being squeezed by apical constriction. Another consequence is that the nuclei move basally as apical constriction progresses. This effect is also attributed to the fact that the cytoplasm is incompressible and the volume of the cell is constant[34].

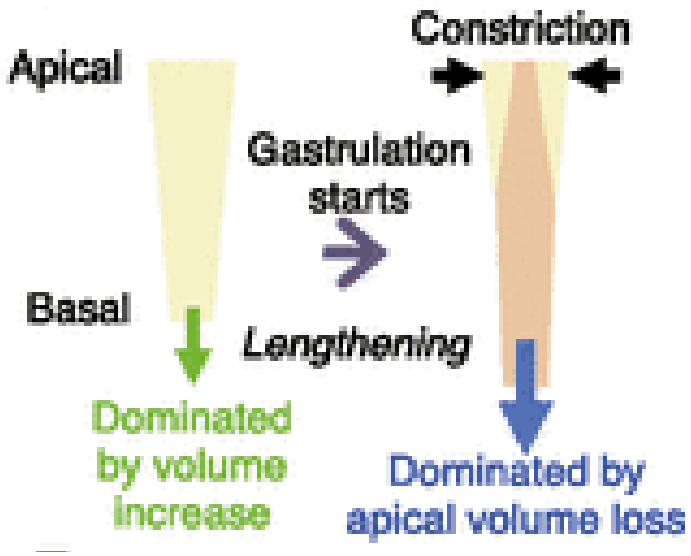

Fig.12 Model of apical-basal lengthening and volume conservation principle. The central mesodermal cells conserve their volume during ventral furrow formation. Thus the apical constriction leads to elongation of the along the apical-basal axis. (Adapted from Gelbart et al [34])

1.4 Junctional remodeling during gastrulation

Cellularization

At the onset of cellularization, a furrow is formed in between neighbouring nuclei. As the new compartments begin to form around nuclei, the membrane shows an asymmetric configuration There is an actin-rich cap on top of the nuclei that forms microvilli and a flat membrane in between the nuclei. The internuclear membrane starts recruiting proteins such as E-cadherin, Par3/Baz, Patj, Dlg and Septins, that form the first junctional complex. Eventually, the furrow deepens and the furrow canal is segregated from the newly formed lateral membrane by the basal adherens junctions (AJs). As the cellularization proceeds, the lateral membranes grow and the basal AJ move with the cellularisation front. At mid cellularization, Bazooka and DE-Cad are recruited into a subapical complex. This marks as the first signs of apical basal polarity in *Drosophila* blastoderm[35]. At the end of cellularisation, there are two junctional complexes; a basal complex at the cellularisation front and a subapical complex containing DE Cad and Baz prominently. Baz is thought to be necessary for recruiting E-Cad to the subapical spot AJs[36].

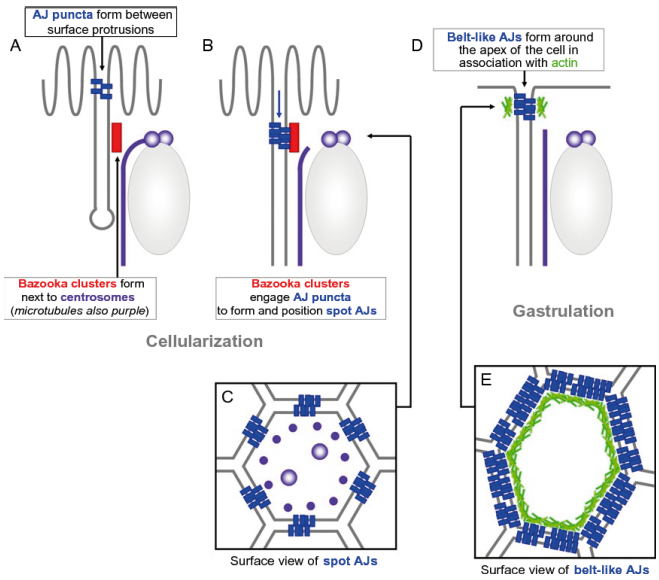

Fig 1.13 Adherens Junctions assembly in Drosophila embryo. A. Separate puntas of E-Cadherin and Bazooka are formed at the onset of cellularization. B. As cellularization progresses, spot AJs are formed comprising of E-Cadherin, Bazooka and other proteins. C. A cross-sectional apical view of the cells and spot AJs. D. A the gastrulation stage the spot junction mature to form a continuous belt-like AJs. (Adapted from Harris et al., 2012 [36])

Remodeling at the onset of gastrulation

The cellularization is completed when the basal actomyosin meshwork contracts and pinches the lateral membrane to form complete cells[37]. At this stage, the basal AJ dissolves leaving only the spot subapical AJ. The subapical spot AJs in central mesodermal cells move apically before the onset of apical constriction. This shift of AJ position is observed exclusively in the mesodermal cell. The AJs remain subapical in lateral and dorsal cells[14,38,39].

Junctional remodeling starts with disassembly of junctions from the initial subapical position. The junctions stay subapical in embryos mutant for *snail,* and they move apical when snail is expressed ectopically. This suggest that the junctional disassembly is dependent on snail. In embryos injected with Baz RNAi, the subapical junctions in ectodermal cells, move apically. Also, in control embryos, Baz is observed to be downregulated before the subapical junction is dissolved. This suggests that the subapical AJs might be destabilized by downregulation of Baz via Snail[14,38,39].

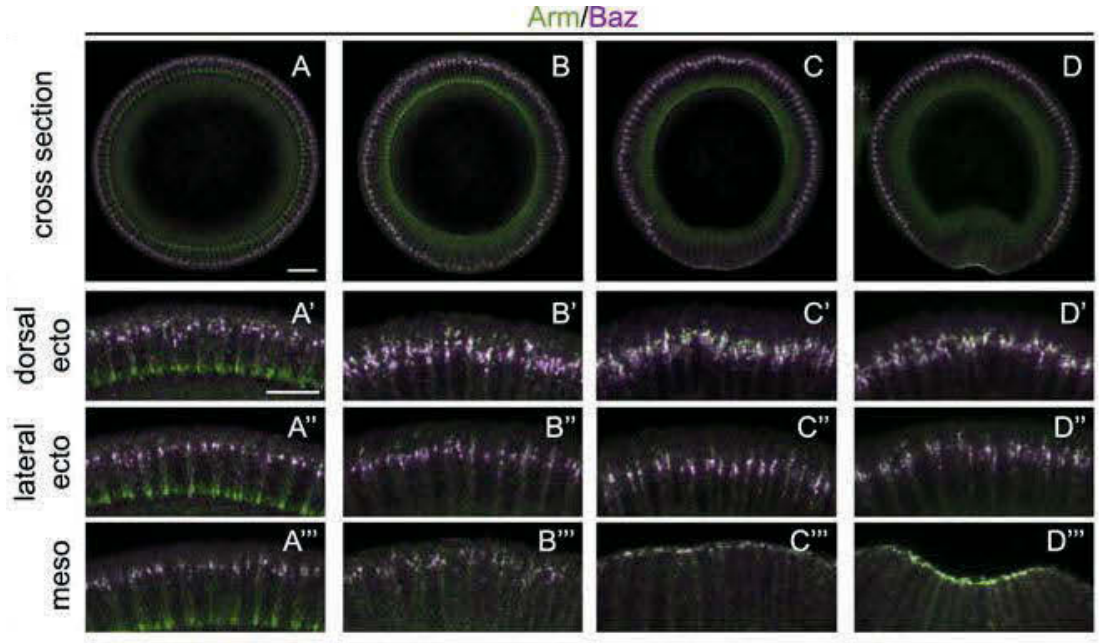

Fig 1.14 Localisation of *Drosophila* β-Catenin and Bazooka during AJs assembly during mid-cellularization (A) , Late-cellularization (B) and Gastrulation. (**C-D**). Localisation of AJs stays subapical in the dorsal cells. A'-D'. and ectodermal cells. A''-D''. but changes in mesodermal cells. The AJs move from initially subapical (A''',B'') to apical (C''', D''') during gastrulation. (Adapted from Weng and Weischaus, 2017 [39])

The ECad and Arm enrichment is not lost upon subapical junctional disassembly. Both proteins show a graded distribution along the apical-lateral membrane. Subsequently, apical AJ is observed in the control embryos. Embryos that lack *traf4* do not reform a stable apical AJ spot but instead show a diffused distribution of ECad and Arm. In embryos that fail to localise RhoGEF2 apically (*cta;T48*), the subapical junctions do not reassemble apically after disassembly. Interestingly, ectopic activation of apical RhoGEF2 via overexpression of fog/cta pathway leads to relocation of Baz and AJs to the apical edge of the cell.

While we understand the mechanism regulating disassembly of sub-apical junctions, the pathway to reassembly of apical AJs is still unclear. There are two theories that try to explain the junctional relocalisation; one theory suggests that there is complete disassembly of subapical junction followed by *de novo* re-assembly at the apical side. The other theory suggests

that the subapical-junctional protein cluster is physically pulled apically because of surface tension generated on apical side by MyosinII.

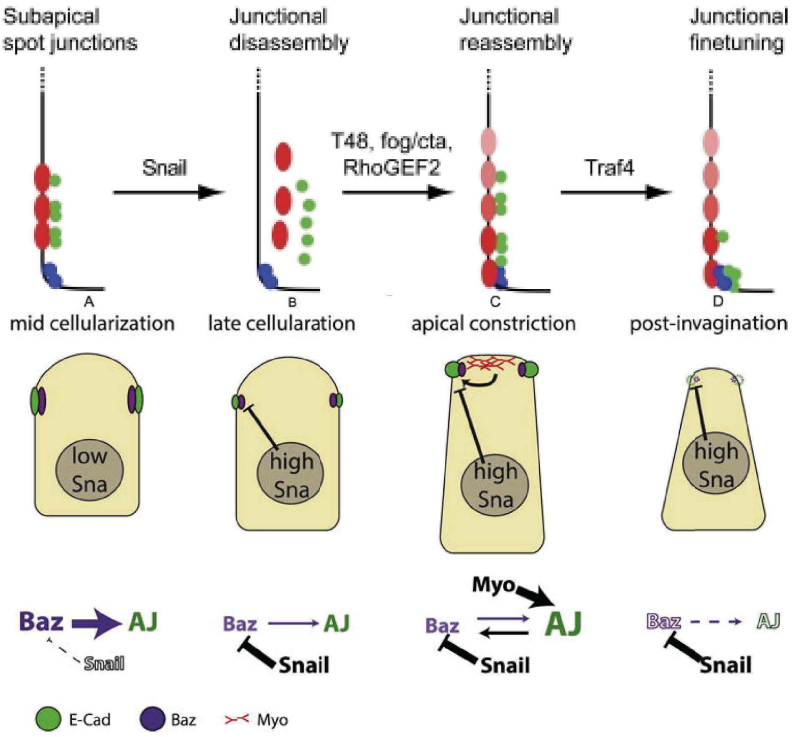

Fig 1.15 Two models for movement of AJs from subapical to apical position in mesodermal cells. (A) A model based on Snail based disassembly of subapical AJs and RhoGEF2 and Traf4 mediated apical reassembly. (B) A model based on down regulation of subapical AJs via Snail and apical stabilization of AJs via MyosinII. (Adapted from Mathew et al., 2011 and Weng and Weischaus, 2017 [22] [39])

1.5 Emergent effects on tissue deformation from cell contractility

Maintenance of tissue integrity and tissue remodeling during development require cell-cell contacts. These cell-cell contacts are central to coordinate individual cell shape changes to have tissue-scale morphogenetic process.

Cell shape changes during ventral furrow formation are cell autonomous and undergo a concerted change in shape to form a furrow. Forces are generated by contraction of apical actomyosin meshwork in the central mesodermal cells. These contractions are propagated across cells via the cell-cell adherens junctions. The AJs are composed several proteins including Shotgun (E-Cadherin), Armadillo (β-catenine), □-catenin, p120 catenine and others. The extracellular domain of Shotgun or the drosophila E-cad t binds to the extracellular domain of neighbouring cell. While Shotgun expression is detected along regions of cell-cell contact, it is found enriched at the AJs. The intracellular domain of Shotgun binds to β-catenin/ α- catenine complex. Connection of the actin cytoskeleton to the AJs primarily happens via α- catenine[40].

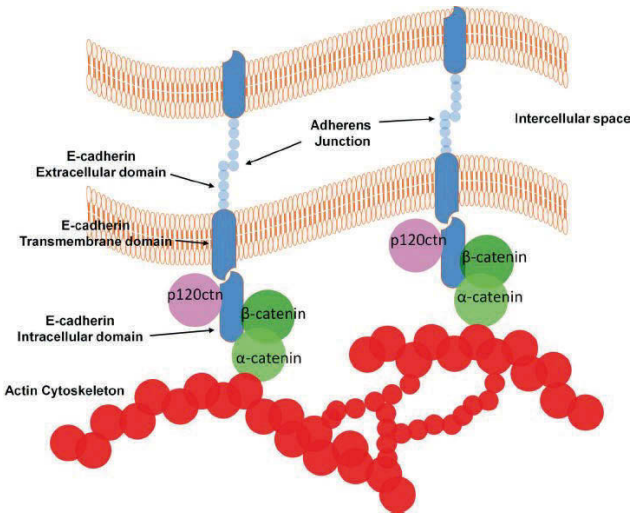

Fig 1.16 Molecules involved in connecting cortical actin meshwork to the AJs. The extracellular domains of E-cad molecules of neighbouring cell interact to form a junction. The intracellular domain of E-cad recruits p120, α-Catenine and β- Catenine that binds to F- actin.

In embryos lacking E-Cad or β-catenine, the apical constriction initiates normally, but as constriction proceeds the actomyosin meshworks in neighboring cells detach. Actin associated membrane tethers are observed connecting actomyosin meshworks of neighbouring cells. Tissue tears are observed where the tethers weaken. These tethers are reduced when the contractility of the mesoderm is reduced[26]. Thus, AJs are required to integrate forces on a multicellular level.

Coordination of constriction

Apical constriction is driven by contraction of actomyosin meshwork. Cells constrict in a stepwise manner via consecutive actomyosin contractions. These actomyosin contractions are cell autonomous and are initially stochastic across the mesoderm. These contractions are stabilized in a ratchet-like manner in cells expressing high amounts of Twist. Cells closest to the ventral midline switch from non ratcheted to ratcheted behaviour in a coordinated manner. The coordination requires Twist activity and might involve fog activity[18]. Study done by Xie & Martin in 2015 observed that ratcheting behaviour stabilizes actomyosin contractions in neighbouring cells. They propose that ratcheting reduces competition between neighbouring cells and helps in multicellular coordination of apical constriction[41].

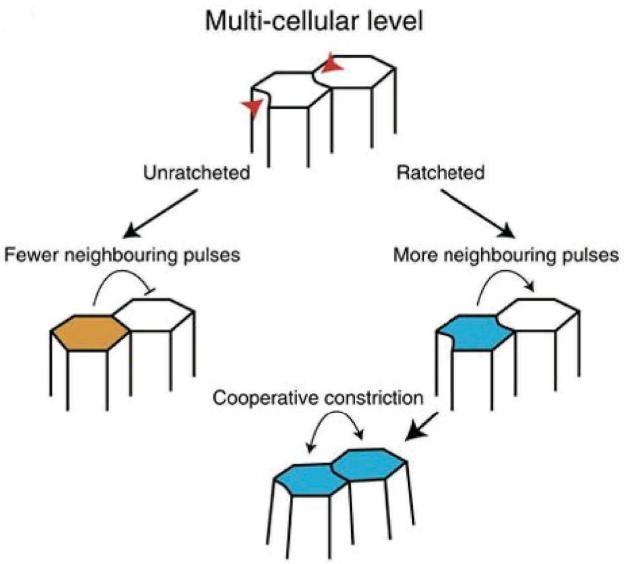

Fig 1.17 Intercellular interaction of constricting cells. Cell with fewer neighboring cells that constrict tend to constrict less frequently that with more neighboring cells that constrict. The ventral cells cooperate with each other (Adapted from Xie and Martin, 2015 [41])

The multicellular gradient

As discussed in section 2, *twist* is expressed as a gradient with highest *twist* expression observed in ventral-most cells. Subsequently this leads to a graded expression of *t48* and *fog.* However, *snail* and the GPCR for fog, *mist* are expressed uniformly in the mesoderm. The current model is that the graded expression of Twist leads directly to a graded activation of apical MyosinII in the mesoderm[12,17]. Expansion of the *twist*-expression domain in embryos injected with *Spn27a*- RNAi leads to expansion of the apical MyosinII gradient. In *Spn27a*- RNAi injected embryos, a wider furrow is formed and is not internalised. In *gprk2* mutant embryos, the MyosinII gradient is disrupted and a wider furrow is formed[42]. Thus, a proper gradient is MyosinII activity is required for efficient furrow formation. As for internalisation, movement of ectoderm and Myosin gradient, both are required[4,12,24]. So, it is not possible to dissociate effects of ectoderm movement and ventral myosinII gradient on furrow internalisation.

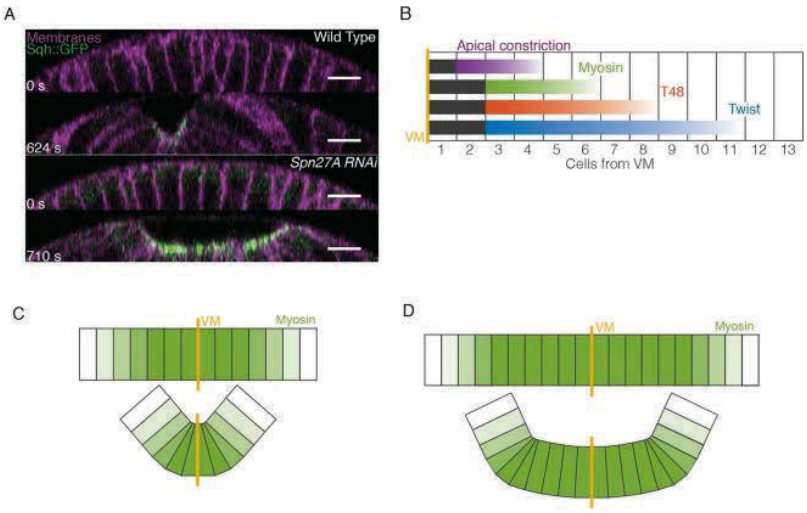

Fig 1.18. Effects of the contractility gradient and tissue geometry on the ventral furrow formation. A. Cross-sectional views of control and Spn27ai embryos labeled with membrane and MyosinII. B. Twist, its downstream target T48, effector molecule MyosinII are graded along D-V axis and gives rise to graded apical constriction. C, D. Modifying the shape of contractile domain affects the MyosinII gradient and leads to formation of a wider furrow. (Adapted from Heer et al., 2017 [12])

Geometry of contractile domain

Central mesodermal cells constrict apically in an anisotropic manner. The cells constrict predominantly along the ventral-lateral direction and stay elongated along the anterior-posterior direction. This anisotropy is due to the fact that the contractile domain is larger along the anterior posterior axis as compared to the ventral-lateral axis. Assuming that cells constrict autonomously, there is larger force along a-p direction as compared to v-l. Measurements of actomyosin meshwork recoil after laser ablation indeed show that there is greater tension built up along A-P as compared to D-V axis[26]. When contractile domain is reduced to an isotropic shape, by either using optogenetics or RNAi injections, the cells constrict isotropically. Chanet S. and colleagues used Spn27a-RNAi and Fat2-RNAi to genetically generate embryos with isotropic contractile domains. In both cases, an isotropic constriction observed. This reinforces the fact that geometry of the contractile domain dictates the geometry of apical constriction[43].

This hypothesis was further validated by Guglielmi and colleagues, who created a tool to locally modulate contractility. They created an isotropic-square shaped contractile domain and observed that cells constricted in a more isotropic manner. However the furrow formation was not blocked.[44] This raises the question whether the shape of the contractile domain is necessary for furrow formation.

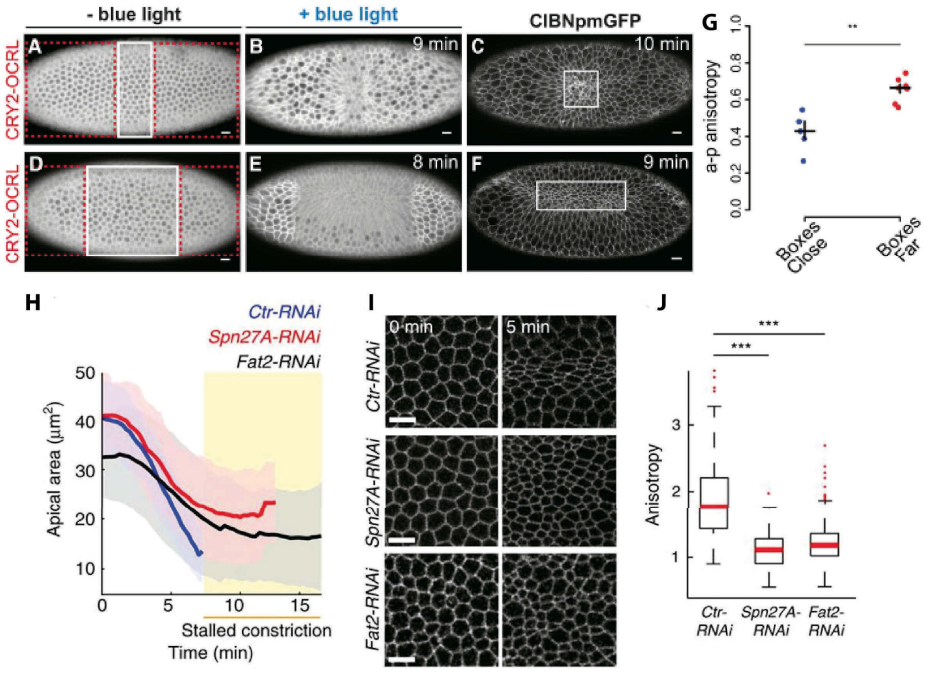

Fig 1.19 Effect of the shape of the contractile tissue on shapes of individual constricting cells. (A) and (D) are stills of embryos expressing CRY2-OCRL and CIBNpmGFP. Upon activation with blue light (red box), the cells loose contractility. (G) When the activation boxes are closer (B,C) the degree of anisotropy is higher that when the activation boxes are far (E,F). (I) Ventral views embryos injected with Control-RNAi, Spn27A-RNAi and Fat2-RNAi at 0 and 5 min after onset of cell constriction. (H) Apical area measurements show a stalled constriction in Spn27A-RNAi and Fat2-RNAi injected embryos as compared to Control-RNAi. (J) Reflecting the shape of contractile domain, the constricting cells show elongation along anterior-posterior axis in Control-RNAi, while the constricting cells in Spn27A-RNAi and Fat2-RNAi injected embryos show isotropic constriction. (Adapted from Gugliemi et al 2015 and Chanet et al 2017 [43,44])

Geometrical feedback to force generation mechanism

Geometry of apical constriction is a cumulative outcome from an interplay between internal force generation machinery and tissue-level tension. However, the relation between the two components is not very clear. Chanet S. and colleagues observed in their study that the cellular actomyosin organisation is dependent on geometry of the contractile domain. In control embryos there are supracellular actomyosin cables that span along the A-P axis. In embryos injected with *Spn27a*-RNAi and *Fat2*-RNAi, the contractile domain is isotropic, there are no supracellular actomyosin cables and MyosinII organises into ring-like structures. To test if these rings are a result of isotropic tensions in the contractile domain, the authors used laser-based ablations to reduce tension along ventral-lateral directions in *Spn27a*-RNAi injected embryos. The laser-induced ablations resulted in anisotropic tissue tension and reoganization of MyosinII ring-like structures into cables[43]. These experiments indicate that formation of MyosinII structures, and subsequent force generation, is dependent on geometry-induced anisotropic tissue tension.

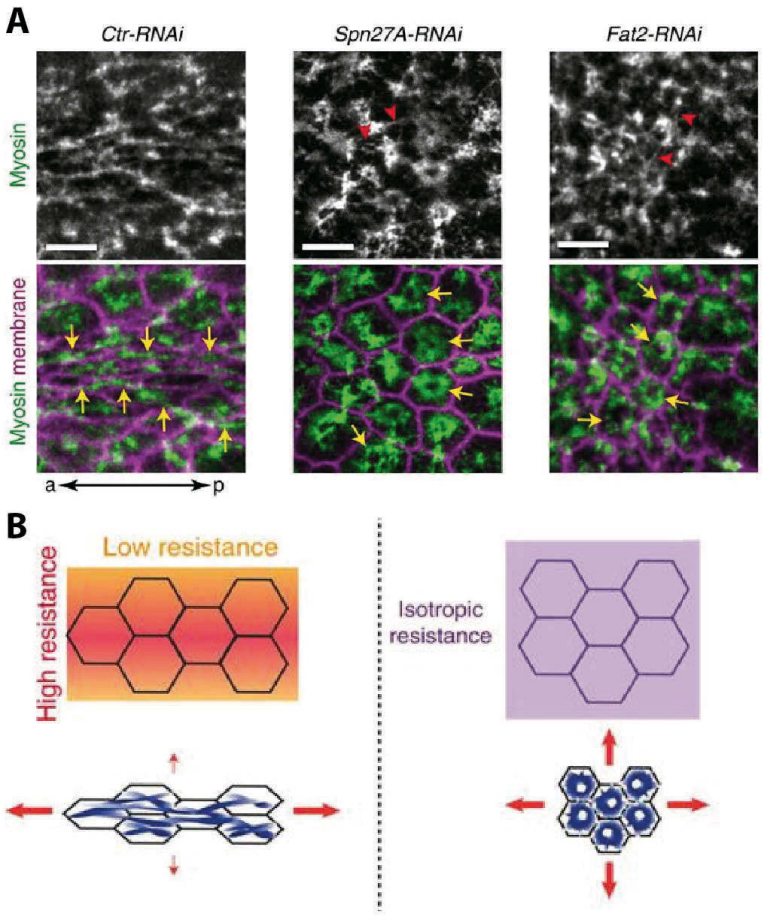

Fig 1.20 Effect of tissue scale tension on organisation of MyosinII filaments. (A) Organisation of apical MyosinII in embryos injected with Control-RNAi, Spn27A-RNAi and Fat2-RNA. MyosinII filaments form cables along the A-P axis in control-RNAi injected embryos and ring-like structures in Spn27A-RNAi and Fat2-RNAi injected embryos. (B) Model of MyosinII filament organisation; under anisotropic tissue stress the MyosinII filaments form fibers orthogonal to low resistance while ring like structure are formed in response to an uniform or an isotropic resistance. (Adapted from Chanet et al 2017 [43])

2. Reconstruction and quantification of 3D cell shape changes during ventral furrow formation

To study the coordination of cell shape changes within the mesoderm, we require 3D reconstruction of cells during ventral furrow formation and internalization. Fig 2.1a shows the conceptual illustration of the workflow for quantifying shape descriptors (e.g. surface area, volume) from raw imaged data. The images are first acquired, then the membrane signal is enhanced by using image processing tools. Then the membrane enhanced images are used to segment the cells in 3D and then track the cells in time. Once we have segmentation results and tracking data, we can extract any desirable cell shape quantities.

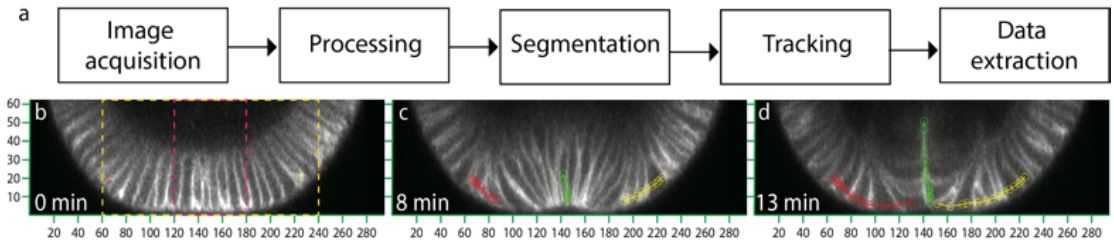

Fig. 2.1 Approach and challenges in imaging lateral mesodermal cells. (a) Schematic of a workflow used for studying cell shape changes in three dimensions. (b-c) Cross sections of a part of the embryo expressing membrane tagged Venus, where the ventral side faces down. X and Y axis present length dimensions. Movements of central mesodermal (CM) cell (green circles) and two lateral mesodermal (LM) cells (red and yellow) on either side of the ventral midline are tracked over time. Cell shape changes and movements of CM cells are contained within the magenta box, but the cell shape changes and movements of LM cells span the yellow box.

2.1 Imaging strategies

There are many challenges in imaging 3D volumes of LM cells during ventral furrow formation. The most important ones are listed below:

a. Measurement of the apical cross-sectional area of the lateral mesodermal (LM) is difficult due to the curvature of the embryo. In the central mesodermal (CM) cells, the change of apical cross-sectional area is nearly orthogonal to the imaging direction. Thus measuring the dynamics of the apical cross-sectional area in CM can be reduced to a two-dimensional (2D) problem. The curvature of the embryo and the LM cells does not allow us to reduce the dynamics of apical area changes in 2D.

b. Fast movements of the LM cells make them difficult to track. The LM cells move rapidly along the radial direction of the embryo while the furrow formation continues to progress and is internalised[42]. The movements are as fast as 10-20 μm/min; hence we need time resolution of at least 1-2 minutes between consecutive time points.

c. Capturing shape changes of LM requires large imaging volumes. To capture the 3D shape changes during apical constriction of CM cells, a volume of 70 x 80 x 60 μm (width along DV * height along AP * depth) covering 8-10 rows of cells along AP axis is sufficient[34]. To capture 3D shapes of 8-10 rows of the LM cells along AP, we require to record a minimum volume of 120 x 80 x 60 μm (width along DV * height along AP * depth) which is ~1.7 times the volume required for CM cells.

d. The shape of the LM cells decreases the quality of the membrane signal. Membranes which are orthogonal to the imaging directions are imaged better than the membranes parallel to the imaging direction. The LM, while expanding apically, have their lateral membrane curved and hence not orthogonal to imaging direction like the membranes of CM cells. The large angle with the imaging direction causes discontinuities in the membrane signal of the LM cells and low signal to noise ratio.

e. High time-resolution requirement limits exposure time and intensity. Limitations on the minimum volume required to image and time resolution

constrain the exposure time for illumination of the embryo. Using higher laser power introduces phototoxicity , so the illumination intensity has to be kept in non-toxic levels.

f. Imaging basal side of the cells is difficult. Imaging deeper into tissue is affected mainly by absorption and scattering due to the tissue. The signal to noise ratio drops as we try to image deeper in the tissue. Deep tissue imaging is a problem while imaging both the CM and LM cells simultaneously.

As a result of all the above factors, the quality of the data is affected. Although conceptually very simple, imaging of shape changes in LM cells is technically challenging. This might be one of the reasons why the LM shape dynamics have not been studied since their first description. We have simultaneously used three imaging strategies to deal with different problems:

Two-photon microscopy - This method yields high contrast images and is suitable for deep tissue imaging. Thus, this method will be used to measure the cell volumes. Datasets were acquired with a voxel size of 0.5 x 0.5 x 1.0 µm3 and temporal resolution of 1 min. Imaging was performed from the ventral side of the embryo up to 60 µm in depth.

SPIM - This method yields high temporal resolution images and is suitable for extraction of apical area dynamics. Datasets were acquired using a single view with a voxel size of 0.19 x 0.19 x 0.75 µm3 and a temporal resolution of 10 sec. Imaging was performed from the ventral side of the embryo up to 90 µm in depth.

MuVi SPIM - This method is the only way to generate 3D volume datasets for the entire embryo.Multiple views were recorded and fused to get an isotropic image of the whole embryo with a final voxel size of 1 x1 x 1 µm3 and time resolution of 60 sec.

2.2 Imaging 3D cell shape changes across the entire embryo

To understand how the forces generated by the CM cells affect the immediate and distant neighbors, I recorded cell shapes changes across entire embryo during ventral furrow formation. Previously, such datasets have been generated, but the imaging conditions were optimized for analyzing only the apical surface of the cells where is imaging quality is good[4]. While these datasets help us understand the apical shape changes of the cells, they ignore the 3D shape changes. Moreover, the analysis completely ignores the LM cells. Recently, the involvement of basolateral membranes has been proposed to play a significant role in the initiation and coordination of cell shapes in *Drosophila* blastoderm[45]. In this section, I will focus on our efforts to generate high-quality datasets for observing 3D cell shape changes and segmenting the entire embryo during ventral furrow formation. I have tried to optimize every step from image acquisition to segmentation for extracting 3D volumes, apical and basal areas, and the apical-basal length.

Images were acquired on Luxendo MuVi SPIM setup using bi-directional imaging and three successive rotations of 60 degrees per time point. Such imaging gives us three pairs (six image stacks) per time point orienting 60 degrees apart. I processed the images by using an open-source software which is being developed by Tobias Rasse, PhD. from Advanced Light Microscopy Facility (ALMF), EMBL. These images are first preprocessed for removing the dead pixels and subtracting the background noise. This step improves the contrast between membranes and the background. Dead pixels are a result of a characteristic noise of the cameras. The dead pixels are replaced by a median of the surrounding pixels. Random noise is further subtracted using the standard a rolling ball radius noise subtraction algorithm.

Thereafter, I imported the preprocessed images into the BigStitcher plugin[46,47] using Fiji software[48]. BigStitcher plugin is used to fuse the six image stacks by using a bead-based rough registration and object-based fine registration. The bead-based registration method gives accuracy up to ~20 pixels, and object-based fine registration provides accuracy up to ~2-4 pixels

for fusion of the six image stacks. Embryos are imaged in a gel that is embedded with fluorescently labeled beads, and the beads are used for rough registration. The landmarks like tricellular junctions and local minima at the center of the cells are used for fine registration. Thereafter, the fused images are deconvolved using BigStitcher. The details of the method are provided in the Methods section. The deconvolution of the images greatly improves contrast near the basal sides of the cell[47]. We expect this improvement in contrast for better segmentation accuracy near the basal side of the cells.

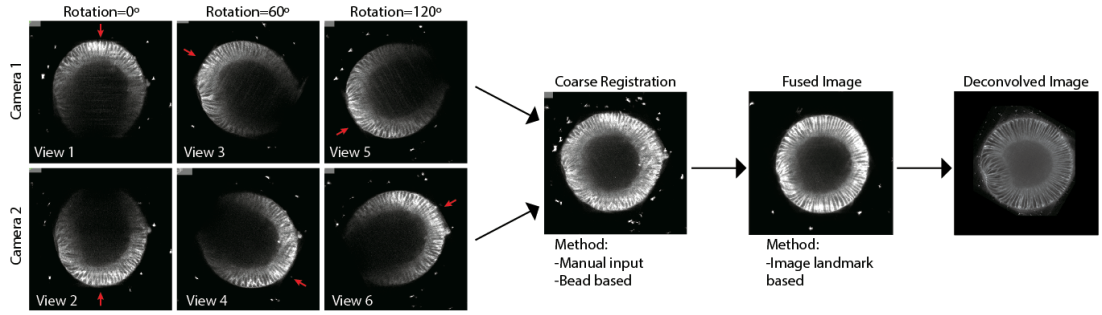

Fig. 2.2 Schematic of the process of multiview fusion and deconvolution. Multiple images are acquired via bi-directional imaging and three rotations of 60 degrees each and are imported into the BigStitcher software. The multiple stacks are initially registered using manual transformations and bead-based registration. Landmarks in the images are further used to register finely and a single fused stack is generated. This fused image stack is then deconvolved using the BigStitcher software.

2.3 Segmentation strategies

To extract measurable quantities like surface area and volume, the images must be segmented. Segmentation of an image means a method where all the voxels belonging to a particular cell are identified and are grouped, while simultaneously leaving out voxels from any other cell or background. There are many open source and commercial software that are available for 3D segmentation (Ilastik, Fiji, ICY, Imaris, ACME etc). Most of these methods are based on 2D and 3D watershed techniques and are ideal for images with high contrast images and high time resolution. These methods have been used for analyzing 3D shape changes in the central mesodermal cells[34], ectodermal cells[45] and dorsal cells[49] because the cells do not move in a large volume and hence fast confocal microscopy is possible. However, methods mentioned above are inadequate to segment the apically expanding lateral mesodermal cells, due to their extreme shape change and rapid movement. I tried using these methods but were not able to get good segmentation results mainly because of the following issues:

a. ‘Open' membranes or discontinuous membrane signal causes fusion of neighbouring cells.

b. The cells haven't completed cellularisation and hence are not 'closed' at the basal side, which leads to the cell fusing with yolk.

c. Some of the methods listed above require input parameters for proper segmentation. It is difficult to find parameters to segment the CM and LM cells simultaneously.

To deal with these specific problems I collaborated with segmentation expert Johannes Stegmaier (RWTH Aachen). We explored several segmentation strategies, and they are listed below

Watershed algorithm-based method

The most common way to segment individual cells is by applying a watershed algorithm. There are many variations and implementations of

watershed algorithms, and we use a marker-based watershed algorithm. Watershed algorithms are effective when the cell boundaries are well defined. 3D segmentation is done by either using a 2D Watershed algorithm on separate Z-slices and combining them into a 3D stack or by using a 3D watershed algorithm. Initially, we segmented individual Z-slices using a 2D watershed algorithm and later fused along the apical-basal direction. This approach works well for most of the cells where there is an 80-90% overlap between neighboring Z-slices. However, in the case of LM cells, the overlap between adjacent Z- slices is as low as 20-30% closer to the base of the embryos. Also, due to the curvature of embryo and LM cells, a cross-section of LM cell along apical-basal direction spans several Z-slices. This further causes problem with the fusion of 2D slices. Thus this method does not prove to be suitable for segmenting LM cells.

Additionally, we used a 3D watershed algorithm for segmentation of the LM cells. We started by automatically generating 3D seeds using local minima (at the center of the cell) at late cellularization stage. At this stage, the cell shape are uniform are the cells do not move. These 3D seeds were then corrected manually, and a 3D watershed algorithm was used to generate the segmentation of the first time point. Segmentation result image of the first time point was eroded mathematically to obtain a 4-5 pixel wide line segment spanning along the apical-basal axis of the cells. These eroded line segments were then used as seed points for the next time frames. This process was repeated for all the time points. In this way, the cell identities (IDs) generated in the first time frame was were propagated in all time frames. Thus, all the cells were segmented and tracked simultaneously.

We applied method described above to the images generated by two-photon confocal microscopy and SPIM. The time resolution between consecutive time points in dataset acquired by two-photon confocal microscopy is not sufficient to faithfully generated intermediate 3D seeds. Low time resolution introduces segmentation and tracking errors. Also, when new cells enter the field of view, the segmentation IDs are not assigned correctly. Incorrect assignment of IDs results in tracking defects.

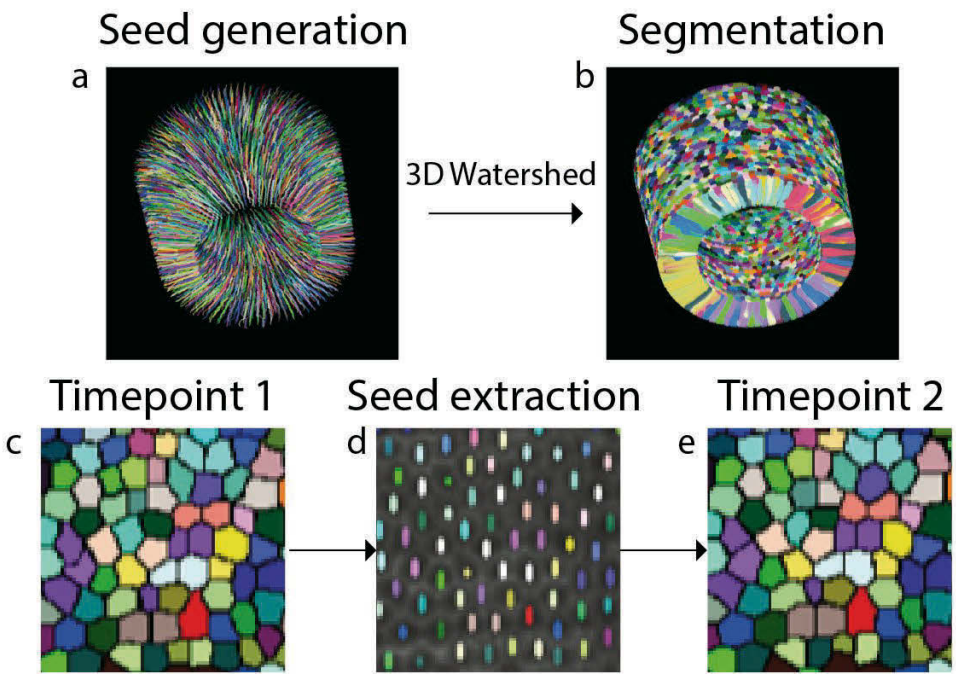

Fig. 2.3 Segmentation workflow showing seed generation and propagation in time. (a) Automatic seeds are generated using local minima to generate 3D segmentation results (b) for the first time point using a 3D watershed algorithm. (c) Magnified view of a cross-section of segmented cells at the first time point. The segmented image is used to extract (d) seeds for which are used to generate 3D segmentation results for the next time point (e). This method conserved the cell identities that are created in the first time point.

The SPIM datasets were acquired at a higher time resolution, and hence we did not expect any tracking errors as long as segmentation was working well. The approach mentioned before has worked well for regularly shaped cells in the early time points and for movements significantly below the time resolutions of our movies. However, this method starts showing segmentation errors at the most apical and basal sides as ventral furrow formation proceeds. Segmentation errors at the apical side of CM cells are due to crowding of membranes. At the base of the cells, the cells are still connected to the yolk via basal canals[50] and thus do not have a well-defined basal signal. This causes segmentation errors at the basal side of the cell. There are additional over- segmentation errors at the basal sides as the signal

is not optimal due to imaging depth. This problem can be partially solved by masking the images.

Image Masking

To improve segmentation accuracy and suppress spurious signals in the background regions and in the auto-fluorescent interior of the embryo, we created a mask for each frame, such that all unwanted image regions were set to black and only the region of interest, i.e. the blastoderm epithelium remained. Masking was done by manually annotating the most apical and basal sides of the cells for 2-6 planes per time frame. After providing the manual input for all the frame a custom written script interpolated in-between the annotations and generated a dense mask which was applied for all time points. Additionally, a high-intensity border is created along the mask to avoid neighbor-fusions introduced by the 3D watershed algorithm.

Convoluted neural network based method

We used a previously developed framework on *Arabidopsis* tissues and used the shape of the Drosophila embryo and blastoderm cells heuristically for improving CNN based segmentation. The low signal to noise ratio at the basal sides of the cells makes detection of the basolateral membranes very difficult. Initially we applied a Gaussian filter to suppress any high-frequency noise in the image, but the membrane signal is still difficult to detect automatically. Then, we trained and applied convoluted neural networks to recognize these weak membrane signals and enhance the signal. After enhancing the membrane signal, the intensity values and the contrast of the membranes improved drastically. Once we have membrane enhanced images, an over-segmentation of the images is performed, *i.e*, the image foreground is partitioned into small fragments of cells (supervoxels) that are later combined to a complete cell. The rationale of identifying supervoxels first is a dimensionality reduction from individual voxels to large groups of voxels that can be processed as a single unit. Moreover, the supervoxel approach

helps to avoid manual parameter tuning by introducing regional boundaries irrespective of the absolute intensity, *i.e.*, even regions with potentially lower signal intensity will be partitioned properly.

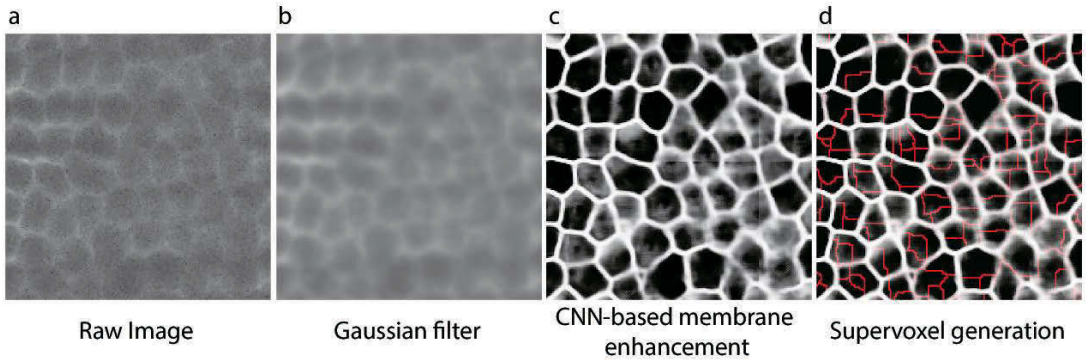

Fig. 2.4 Workflow showing CNN-based membrane enhancement and supervoxels generation from weak membrane signal images. (a) Cross section of cells along apical-basal axis and 40 microns from the apical surface. (b) Gaussian filtering reduces high frequency noise and smoothens the image. (c) CNN are used to detect and enhance membrane signal. (d) All local minimas are used to over-segment the image in to supervoxels. Red lines are the boundaries of the supervoxels

To merge the resulting supervoxels into complete cells, the interfaces between touching supervoxels are categorized as either correct or incorrect. This was achieved by using prior information of the shape of the cells that favors merge in the radial direction. We also used convoluted neural networks (CNN) that are trained on manual annotations for generation of fusion probabilities . The CNN yields a probability map for each image with probability values close to 1 for valid plasma membranes (PM) and probability values close to 0 for background regions. The probability map is then used to compute the average probability of voxels contained in each interface between neighboring supervoxels. If the interface probability falls below a threshold of 0.5 it is classified as incorrect and otherwise as correct. Correct interfaces are kept and incorrect interfaces are iteratively collapsed until the final segmentation is obtained.

2.4 Cell volume measurements using confocal microscopy

Two-photon confocal microscopy has been used to study 3D shape changes during apical constriction, germband extension and dorsal fold formation in the early *Drosophila* embryo. To generate a detailed description of the LM cells using two-photon microscopy, embryos expressing GAP43::Venus were imaged to visualize the cell boundaries. Instead of imaging the entire length of the embryos, the central 30 % part of the embryo along the A-P axis was imaged to improve the time resolution of the consecutive time points. The images were then masked manually using a custom Matlab script as described previously. The manually masked images were then used for segmentation, and to reconstruct the 3D volume.

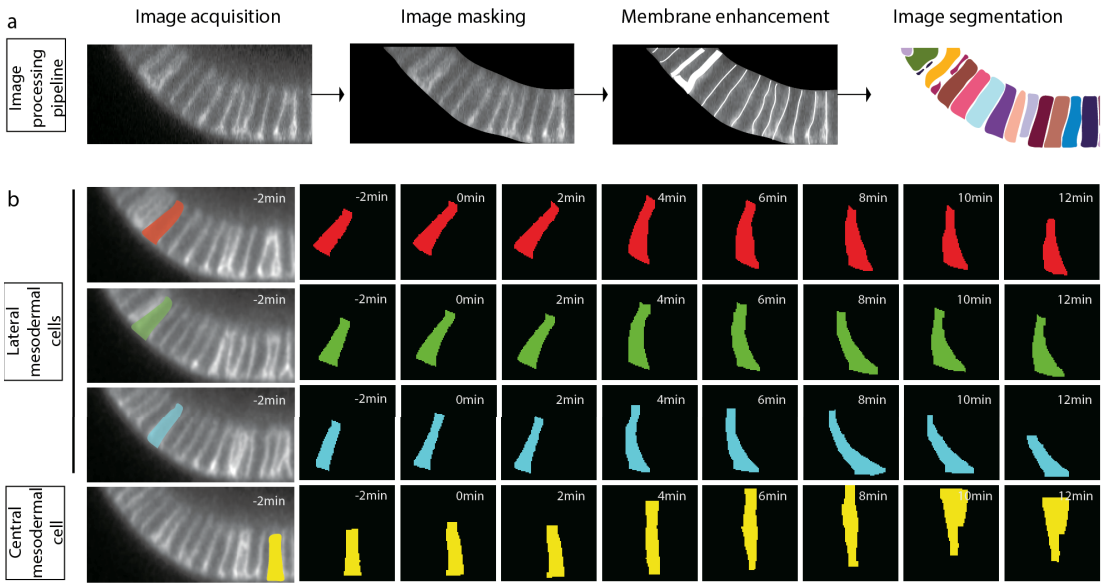

Fig. 2.5 Workflow for quantifying cell shape changes during ventral furrow formation. (a) 3D stacks are acquired over time and a 3D region of interest is selected using manual masking. The masked images are used for segmentation and 3D surface and volume reconstruction. (b) Reconstruction of cell shape changes in three LM cells(LM; red, green and cyan) and a CM cell (CM; yellow). Apical surface faces towards the bottom and basal surface towards the top of the images. The LM cells expand apically and the CM cells constrict apically. The positions of the four cells are represented in the corresponding position in the embryo (rightmost column)

Segmented images were used to quantify the cell shape changes during ventral furrow formation. Summation of all the voxels of cells gives the volume of the cell. We measured volumes of the cells in the region of interest and tracked them overtime. Fig 2.6 shows quantifications for volume changes for the mesodermal cells over time. The distribution of cell volumes over time is plotted in Fig 2.6 (d). The plot shows that the volume stays constant from onset of gastrulation to furrow invagination.

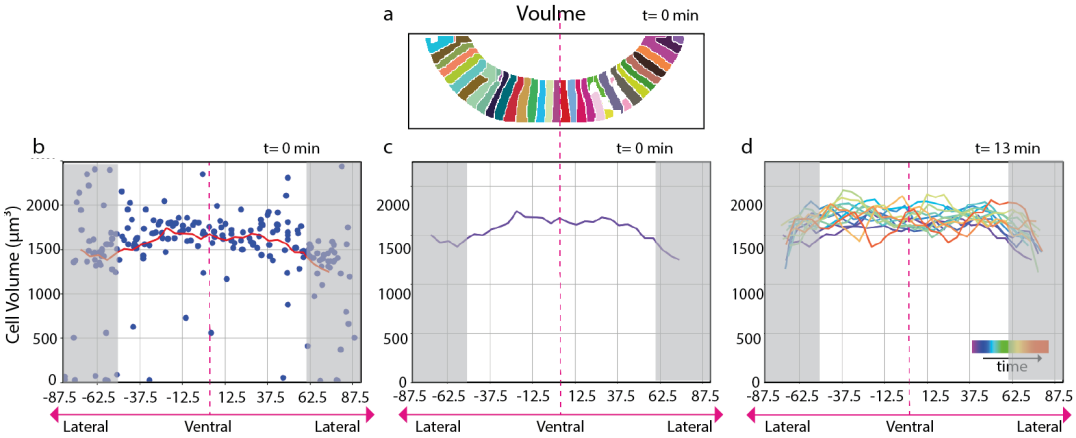

Fig. 2.6 Volume changes in mesodermal cells. (a) Cross-sectional view of a segmented embryo with ventral facing down and lateral on the side . The red dotted line marks the ventral midline (VM) in the entire figure. In the plot (b) volumes of the individual cells (blue dots) comprising the middle 30% part of an embryo along the anterior-posterior axis and their mean (red line) is plotted against position of the cells from the ventral midline along the ventral-lateral axis (VL). The lateral most cells (grey box) in the analysis have multiple segmentation errors and are thus excluded for interpretation of the plots. (c) The average volume along the V-L axis at onset of gastrulation. (d) Distribution of volume along VL axis over time. The first time-point is coded in violet and the last time-point in red.

2.5 Extraction of the surface peel and quantifying the apical area changes

The force generating actomyosin machinery and the adherens junctions are located at the apical side of the cells. Thus we expect the effects

of force generation and transmission to be most obvious on the apical areas of the cells. So we wanted to extract the apical surface dynamics using SPIM imaging. The datasets generated using two-photon microscopy do not have sufficient time resolution to track the majority of the cells. To get better tracking of the cells we used selected plane illumination microscopy (SPIM). We imaged from the ventral side of the embryo with a time resolution of 12 seconds. The data sets have low contrast at the basal sides so are not suitable for 3D segmentation but the contrast is sufficient at the surface of the embryos to quantify the apical area changes of the cells.

To extract the apical surfaces, we wanted to define the shape of the embryo and specifically extract the apical surface. We first used a Gaussian filter (8 px radius) to blur the membrane signal and get a rough shape of the embryo. The rough shape of the embryo was inferred from the blurred embryo signal was used to generate distance transform maps. Using distance transform maps, we isolated the apical surface of the embryo (See Methods for details). The apical surface is however a two-dimensional surface on a three-dimensional object. Thus, we projected cartographically the apical surface on to a 2D flat surface. The projections were then segmented and individual cell movements were tracked. This dataset captures the apical dynamics of the central and lateral mesodermal cells until the ventral furrow deepens and starts to invaginate. In Fig.2.7 (b-c) the apical area measurements of the CM and LM cells is plotted against time. We observe that the CM cells reduce their apical area and the LM cells are observed to increase their apical area as ventral furrow formation proceeds. There is a strong correlation between the apical area reduction and increase in the mesodermal cells.

To observe the average behavior of the mesodermal cells, we plotted the apical area as a function of their position along the dorsal-ventral (DV) axis. We fixed the position of the ventral midline at zero. The cells were binned in a bin size of 10 microns and mean was used to represent the bin. The apical areas of the CM cell show a gradient along the DV axis with the cells closest to the ventral midline with least area and increasing areas in the lateral cells. The apical areas of the LM cells do not follow the same gradient.

We analyzed area changes in three rows of the apical expanding cells. The mean and standard deviation of the apical areas of three rows of apically expanding cells was plotted(FI. 2.7 (e)). The apically expanding LM cell row which is closest to the ventral midline starts expanding first and has expanded the most among the three rows of the clls. This behavior is also apparent in the cross-sectional views of the embryo.(Fig. 2.7 (d), green box; (f))

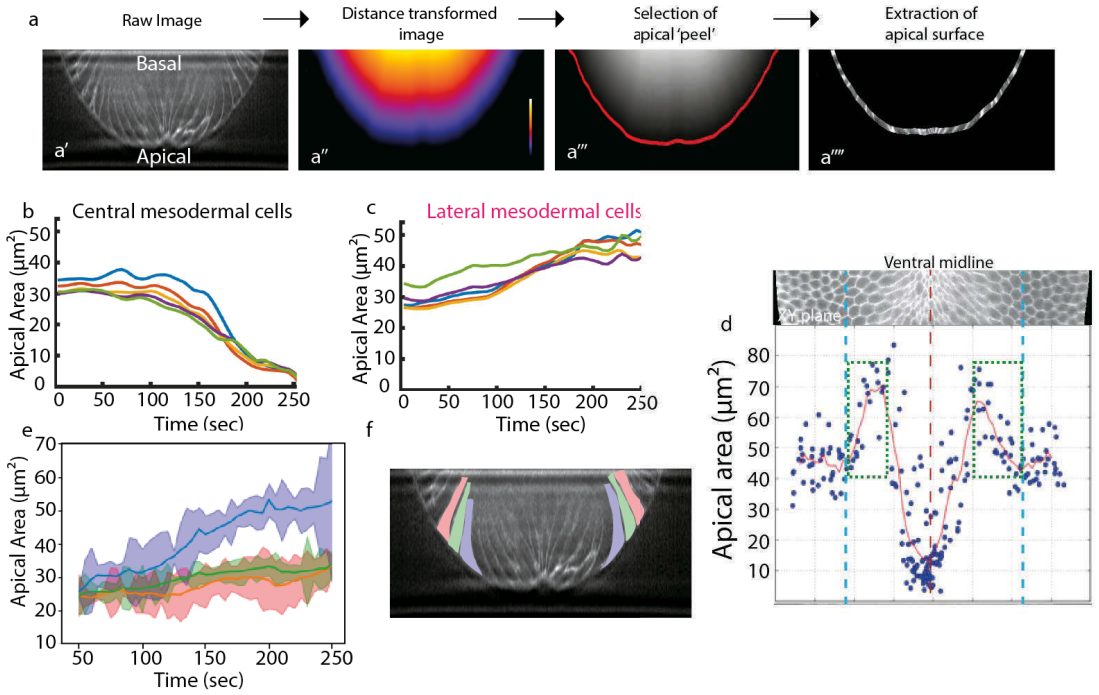

Fig. 2.7 Workflow showing extraction and quantification of apical surfaces of the cells. (a) Images acquired using single view SPIM are blurred using a Gaussian filters and are then distance transformed. An apical mask is generated from 2-3 pixel wide selection from the surface of the embryo. The apical 'peel' is used to extract the apical surface of the embryo. The apical surface is then projected cartographically and segmented semi automatically. (b,c) The central mesodermal cells reduce their area and the lateral mesodermal cells increase their apical area. (d) Plot showing apical areas of cells (mean) and mean apical area (red line) against the ventral - lateral axis. Vertical dashed line indicates the ventral midline in the XY plane (above the plot), in the plot and in the XZ plane (below the plot). Blue dashed lines indicate the mesectoderm boundary. At the onset of ventral furrow formation, the cells closest to the ventral midline have the least areas, then the apical areas increase towards the lateral direction. The LM cells closest to the ventral midline (VM) has the highest apical area and the more lateral LM cells have smaller areas (d, green box). (e) Dynamics of mean apical area and standar deviation of the three apically expanding cell rows are plotted. The LM cell row closest to the VM begin to expand earlier and

have the larger apical area than the more lateral cell rows. (f) A cross section of embryo expressing GAP43::mCherry at the onset of ventral furrow formation showing the three rows of apicall expanding cells.

2.6 Embryo-wide 3D shape changes

The previous two approaches (section 2.4 and 2.5) are limited to study only the ventral part of the embryo. To analyze the three-dimensional shape changes in the entire embryo we used datasets that were imaged using multiple views, fused and deconvolved (section 2.2). We used CNN-based membrane enhancement and 3D segmentation to 8-10 rows of cells along the AP axis of the embryo. We measured the volume, apical area, basal area and the apical-basal lengths from the segmented datasets. Multi-view image acquisition is slower than single view acquisitions and thus the cells are more difficult to track.

Fig 2.8 shows quantifications of 3D measurements for a single time point at the initiation of furrow formation. The cross-section of the embryo is divided into angles and the ventral midline is fixed to be zero. Thus the cells in between ~0-40 and 320-360 degree are the mesodermal cells, the cells approximately between 150-210 degree are the dorsal cells and the cells in between the mesodermal and dorsal cells are the ectodermal cells.

Volume , apical area, basal area and apical-basal lengths are plotted on a circular coordinate system. Angles represent position of the cell with respect to the ventral midline and distance from center of the plots represents magnitude of the quantity that is plotted. The volumes of the cells do not show a strong difference in distribution along the DV axis. The apical areas of the ventral most cells (330-30 degrees) show reduced apical areas and the cells around ~30-40 degrees and ~320-330 have increased apical area than the rest of the embryo. The apical-basal length of the mesodermal cells is larger than the rest of the embryo.

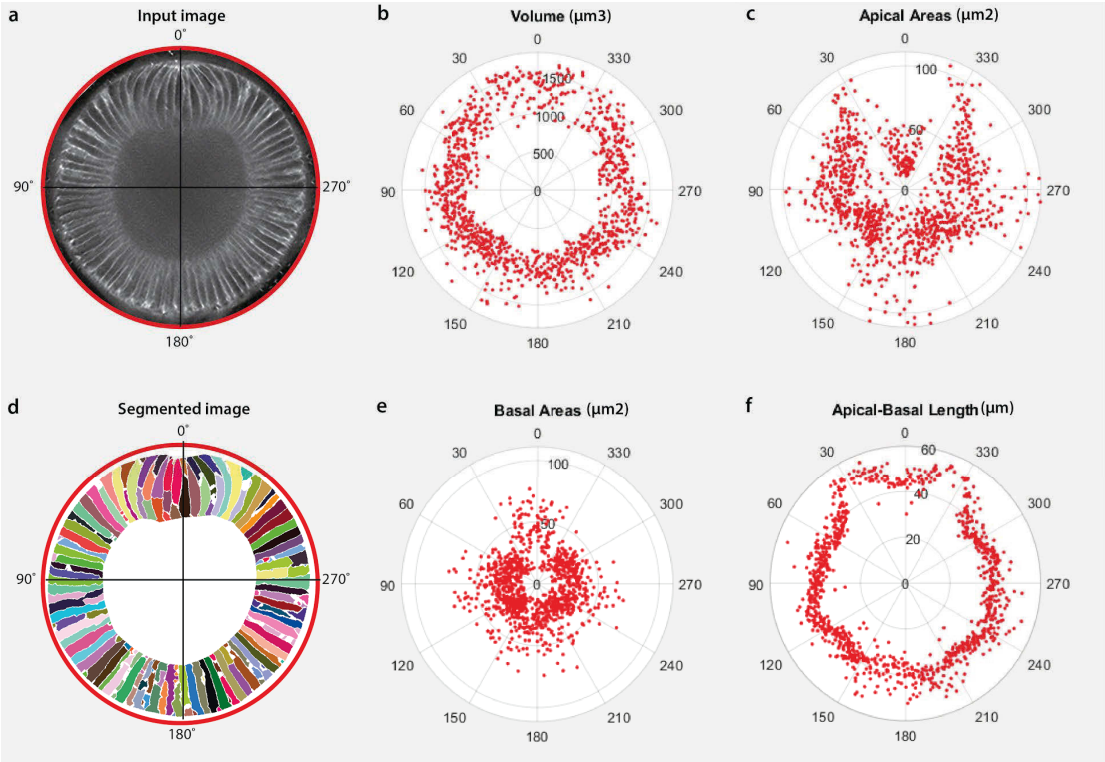

Fig. 2.8 Embryo-wide analysis of 3D segmentation of the cells. (a) Cross-section of an embryo that is imaged from multiple views, fused mathematically and deconvolved. The embryo is presented in an angular coordinate system where 0 degree marks the ventral midline. (0 degree=ventral, 180 degree=dorsal) (d) 3D Segmentation result for the entire embryo is used to quantify cell shape descriptors. In each of the plots, angles correspond to the position of cells in the angular coordinate system. Distance from the center corresponds to the magnitude of the measurements. (b) The volume of the cells is graded along DV axis of the embryo. The ventral cells have larger volumes than the dorsal cells. (c) Ventral most cells have reduced areas and there is a peak around 30 and 300 degree which corresponds to the LM cells. (e) Most of the ventral cells have larger basal areas as compared to the rest of the embryo. (f) The ventral cells are more elongated along the apical-basal axis than the rest of the cells.

Our observation on the cell shape changes of the CM using the imaging and segmentation methods described above, are consistent with the measurements done earlier. Thus we have a method to reconstruct the entire 3D shape changes of the entire Drosophila embryo during ventral furrow formation.

3. Actomyosin organization in lateral mesodermal cells

The cell shape changes in the CM cells are driven by an apical supracellular actomyosin meshwork[18,25,26,51]. To understand how the forces generated in the CM are transmitted to the LM cells, it is necessary to understand localisation and dynamics of actomyosin in the LM cells. In this section I have used SPIM and confocal microscopy to observe the MyosinII dynamics in the LM cells during ventral furrow formation.

3.1 MyosinII distribution in mesodermal cells

To observe the embryo-wide distribution of MyosinII, embryos expressing GAP43::mCherry (membrane) and sqh::GFP (MyosinII) were imaged using MuVi-SPIM with two simultaneous imaging directions and two rotations (90 degrees each). Images were then mathematically fused (see material and method for details) and the cross-sectional views of the resulting images are represented in Fig. 3.1. Consistent with the previous reports, I observed a changes in MyosinII distribution from cellularization to the gastrulation stage. During cellularization, MyosinII is localized at the basal side of cells, where it colocalizes with the cellularizing front[18]. At the onset of gastrulation, MyosinII is localized at the basal side and starts to accumulate at the apical side of cells (blue arrow). As apical constriction in the CM cells progresses, there is an increased accumulation of apical MyosinII in only the ventral cells (Fig. 3.1 (c)).

To quantify the MyosinII intensity distribution across the mesoderm I measured intensity of sqh::GFP along a 3-pixel wide line passing through the apical side of the mesodermal cells. To accurately mark the boundary between mesoderm and ectoderm, we backtraced the cells that meet the middle after mesoderm internalisation; these cells are the Mesectodermal cells (ME, yellow dot). The intensity of MyosinII is graded along the ventral-lateral direction with the maxima at the ventral midline. The GAP43::mCherry

signal also shows a graded pattern, but it is mild as compared to the MyosinII signal, indicating that The intensity of MyosinII in the LM cells is less than in the CM cells. In the Fig. 3.1 (e) MyosinII intensity in the mesoderm is normalised to the membrane signal and plotted.

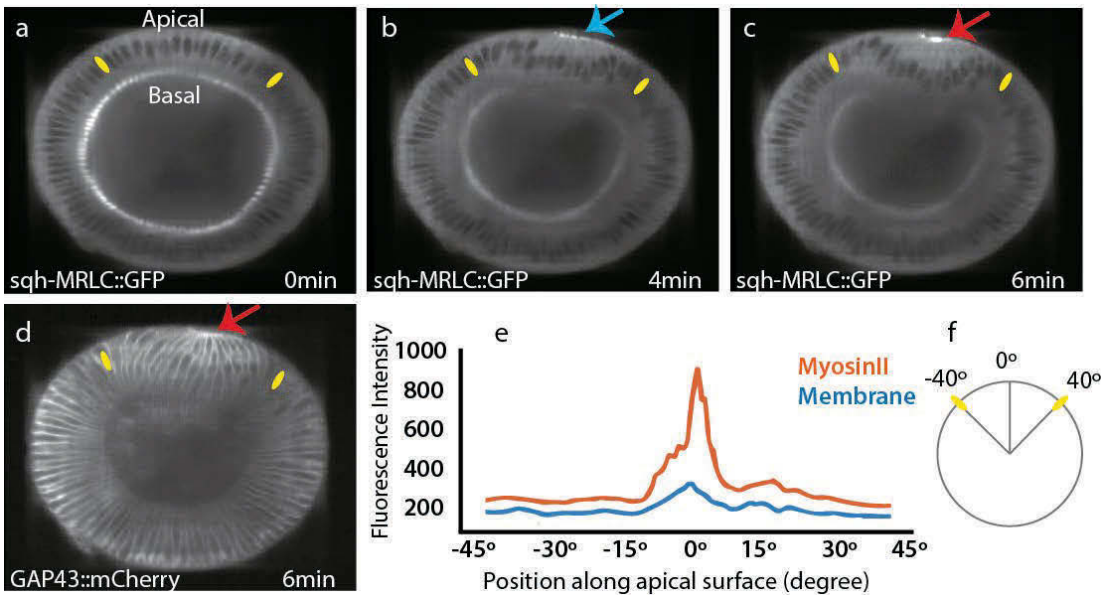

Fig. 3.1 Localisation and quantification of apical MyosinII. The localization of MyosinII at late cellularization (a) and as gastrulation progresses (b,c) as seen in a reconstructed cross-sectional view of an embryo. The cross-sectional view was assembled by fusing images acquired with MuVi SPIM in which two simultaneous views and two rotations were used. MyosinII is localized at the basal side of the cells until; cellularization stage (a) and redistributes to the apical side (blue arrow) in mesodermal cells at the onset of gastrulation (b). (e) Measurement of MyosinII intensity during furrow formation normalized to the membrane marker (d) reveals a gradient of apical MyosinII. Yellow cells mark the boundary of the mesoderm.

To observe localization of apical MyosinII, actin and upstream activating molecules, I used confocal microscopy. Initially, I imaged embryos expressing the actin-binding domain of Utrophin fused to GFP (UtrABD::GFP) and Sqh fused to mCherry (sqh::mCherry). The embryos were imaged from ventral direction. The fluorescence in the first 4 microns from the vitelline membrane was observed and the stacks were z-projected (Max projection). The localization of actin and MyosinII were observed in the same embryo at different time points. Same embryo was used to observe the actomyosin

localization associated with the shape change. In the CM cells that have constricted apically, actin and MyosinII both are enriched in the middle of the cell (medial; Fig 3.2 a-a'''). In LM cell that has expanded apically, actin is enriched along the junctions and the cortex while MyosinII shows a scattered enrichment along the junctions (Fig 3.2 b-b'''). In the ME and the ectodermal cells actin and MyosinII are both enriched along the junctions at the time where mesectoderm is closing the furrow (Fig 3.2 c-c''' and d-d''').

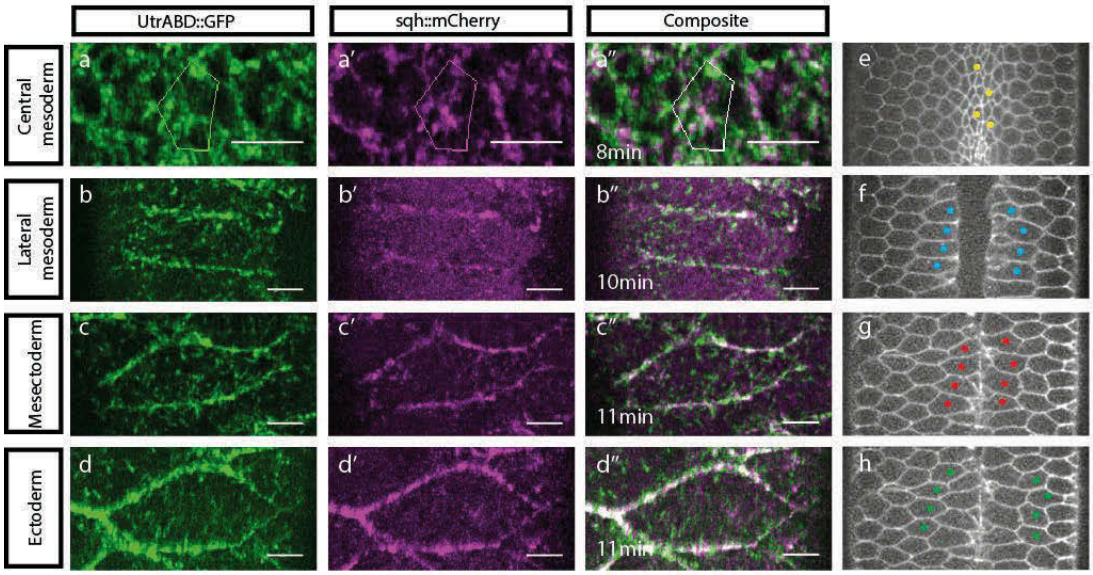

Fig. 3.2 Localisation of F-actin and MyosinII in mesodermal and ectodermal cells. The images are taken sequentially, depict different developmental times and are from the same embryo. The positions and corresponding shape changes in the central mesodermal, lateral mesodermal, mesectodermal and ectodermal cells are shown in e-h respectively. F-actin and MyosinII is localized preferentially to the medial part in CM cells (a-a") and along the junctions in the LM cells (b-b"). There is a stronger activation and more prominent localization of F-actin and MyosinII along the junctions in the mesectoderm (c-c") and ectoderm cell (d-d"). Scale bar is 5 micrometers

The CM cells and ectodermal cells are reported to undergo cycles of assembly and disassembly of MyosinII coalescence[25,32]. To find out if LM cells show a similar behavior, embryos expressing sqh::mCherry and Spider fused to GFP (Spider::GFP) were observed. The embryos were mounted with the

area roughly halfway between ventral and lateral side facing the objective. We observed that there are instances of assembly (Fig. 3.3 a,b) and disassembly (Fig. 3.3 c,d) of coalescence of medial MyosinII. There is no net obvious increase in medial MyosinII levels in the LM cells which is also evident in the cross-sectional views(Fig. 3.1 (c)) and apical views (Fig. 3.2 (b')). With the current techniques, it is not possible to track MyosinII coalescence and the entire apical area changes simultaneously of the LM cells with necessary spatial and temporal resolution due to the size of the LM cells and movement of the cells out of the planes of interest.

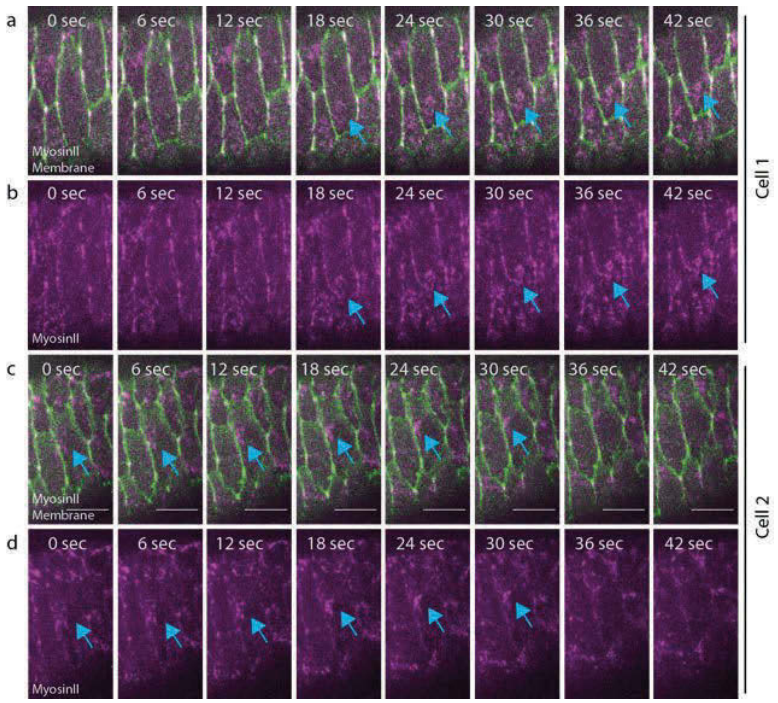

Fig. 3.3 Examples of assembly and disassembly of apical-medial MyosinII coalescence in LM cells. (a,c) Merged images of MyosinII::mCherry (Z-projection, 5µm depth; Magenta) and Spider-GFP (single Z slice, 2µm deep; Green). Assembly (b) and disassembly (d) of apical MyosinII coalescence (blue arrow). Scale bar is 10 micrometers

3.2 Localisation of activators of apical MyosinII

To explore how the localization of MyosinII is established in LM, we analyzed the localization of its upstream activator, RhoGEF2, and RhoA. To visualize active Rho1, we imaged RhoA binding domain of Anilin, fused to GFP (AniRBD::GFP). AniRBD::GFP is used as a RhoA sensor[32]. To visualize active RhoGEF2, we used endogenously GFP tagged RhoGEF2[23]. AniRBD::GFP co-localizes with MyosinII medially and junctionally in constricting CM cell. In apically expanding LM cells, AniRBD::GFP localizes along the junctions. AniRBD::GFP co-localizes with MyosinII medio-apically in constricting CM cell. In apically expanding LM cells, AniRBD::GFP localizes along the junctions.

In the CM cells RhoGEF2 is localised to the medial and junctional domains of the cell. In the LM cells, RhoGEF2 is totally excluded from the medial domain of the cells. There is a junctional signal of RhoGEF2 in the LM cells, but the signal is weaker comparable to the signal in CM cells. The junctional levels of RhoGEF2 in LM cell at the apical side are similar to the levels of junctional RhoGEF2 at the subapical domain of LM cells. These observation indicate that there is a weak activation of RhoGEF2 along the junctions in the LM cells.

RhoA and RhoGEF2 are either excluded or not stabilized in the medial domain of the LM cells. They might be diluted out due to the increased apical area. Alternatively, the absence of RhoA and RhoGEF2 from the medial domain might be due to low twist activity.

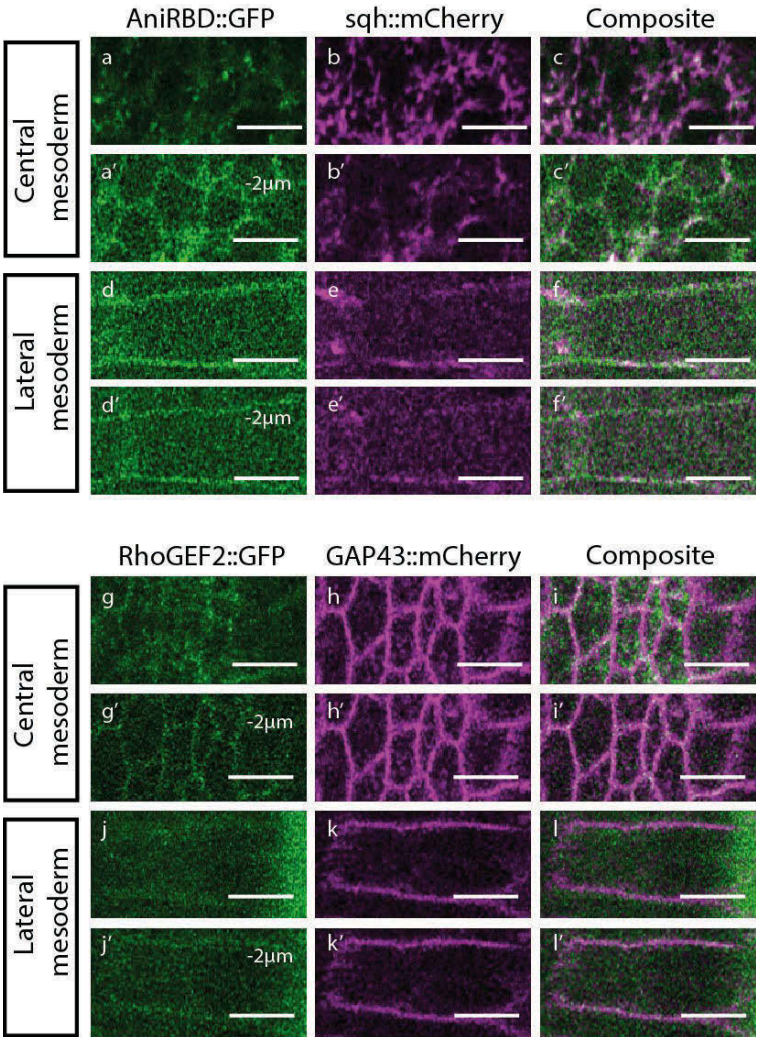

Fig. 3.4 Localisation of the Rho1 sensor (AniRBD) and RhoGEF2 in the central and lateral mesodermal cells. Z-projection of first 2 microns and a single Z-slice 2 microns below the apical side (n,o red line) are shown. (a-c,a'-c') In the CM cells RhoA is localized to the medial and junctional domain. (d-f,d'-f') In LM cells, RhoA localizes to the junctional domain. (g-i,g'-i') RhoGEF2 is localized to the medial and junctional domain in CM cells.(j-l,j'-l') RhoGEF2 is localized to the junctional domain in the LM cells

3.3 Measurement of cortical tension across the lateral mesodermal cells

Forces driving the ventral furrow formation are generated by apical constriction of the CM cells. It is not clear how these forces are transmitted to the LM cell , the immediate neighbours of apically constricting cells. To measure if the LM cells transmit any force, we wanted to measure cortical tension across the LM cells at the onset of ventral furrow formation

Recoil measurements after laser dissection is a widely used technique and it has been applied in *Drosophila* blastoderm[4]. I measured the meshwork recoil during the first minutes of furrow formation in CM and LM cells. Infrared pulsed laser was used to ablate the actomyosin meshwork at the apical side of the cells and the recoil was measured using Particle image velocimetry (PIV). We analysed the actomyosin meshwork recoils along the DV axis only. Velocities in the first 10 seconds were only used for the analysis. It is well established that the initial meshwork recoil corresponds to the tension (or stress) in the tissue[52,53]. I compared the actomyosin meshwork recoils in the CM and LM cells. My measurements reveal that the actomyosin meshwork recoils faster in the CM than LM cells. The Kymographs in Fig. 3.5 (g,h) are plotted along a line passing through the laser dissected ares (orange). The CM cells recoil faster than LM initially but then do not recoil further. The LM cells recoil slower than LM cells initially but are observed to continue deforming.

The cortical tension measurements in the LM cells indicate that cells are not completely compliant and show a certain degree of resistance. Also the LM cells do not expand simply like an elastic sheet and they dissipate the contractile force from the CM cells while deforming. Thus we think that LM cells show viscoelastic properties

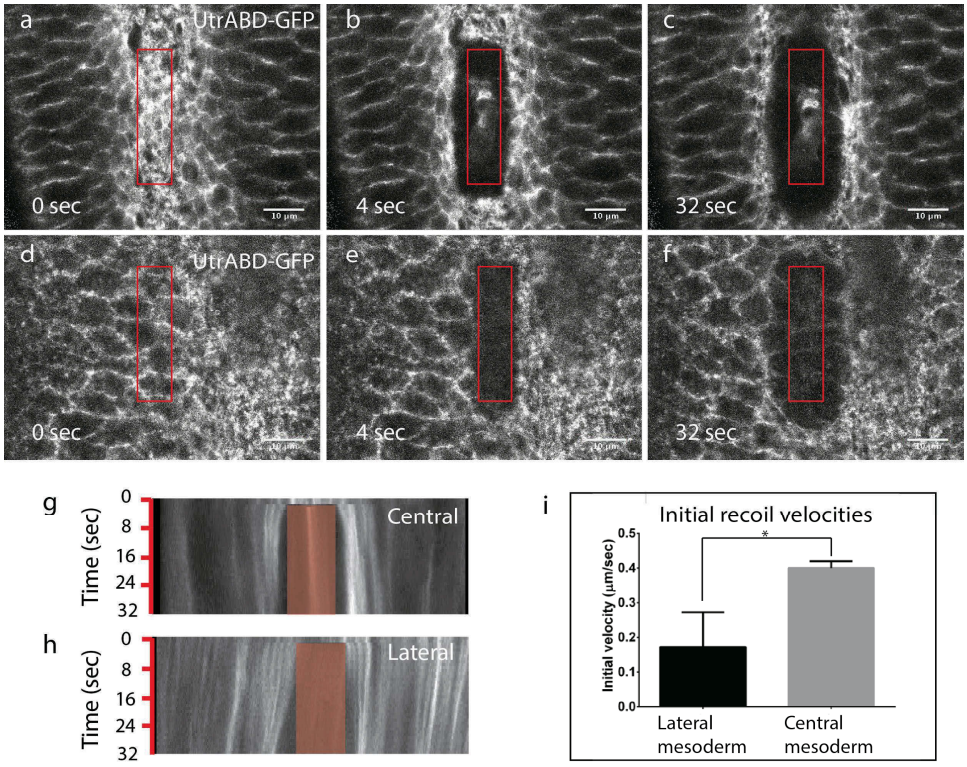

Fig. 3.5 Experimental measurements of initial recoil velocities of actin meshwork after laser dissection in the central (a-c) and lateral (d-e) mesodermal cells. An infrared pulsed laser was used to laser-dissect actin meshwork (red box) and the recoils were measured using Particle Image Velocimetry (PIV) analysis. (g,h) Kymographs along a horizontal line passing through the center of the laser-dissected region. (i) Quantification of initial recoil velocities (0-10 sec) in central and LM cells. (*p<0.01, non parametric t-test, n=8)

4. Functional analysis for coordination of cell shapes in mesoderm

There is a virtual boundary between the LM and CM cells in terms of their cell shape behaviour. The ectodermal cells adjacent to the ME cells do not change their cell shape and stay fixed during the apical constriction and only start moving during furrow internalisation. The LM cells display unique biophysical properties that are different from the ectodermal and the CM cells. The LM cells are part of the mesoderm and express *snail* and *twist*, however they lack expression of *fog* and *t48.* In this section we want to understand how the patterning of snail, twist and downstream targets might lead to generation of a virtual boundary between the CM and LM cells.

Cell shape behaviors within the mesoderm of in *snail, twist* double mutants are impaired[1]. CM cells do not constrict, and LM cells do not expand. Thus either LM cells are dependent on CM cell apical constriction or LM cells require snail or twist for apical expansion. However in embryos mutant for *rhogef2*, *rho1*, *Rho kinase (rok)* or double mutants for *cta* and *T48,* the signaling pathway from Fog to the activation of MyosinII is interrupted and consequently no ventral furrow forms[14,18,54,55]. No elongation of LM cells is seen on sections of fixed embryos or on scanning electron microscopy (SEM) images. This hints that the contractile forces generated in the CM are necessary for apical expansion of the LM cells. In the following section, we have used genetic, biophysical and optogenetic tools to test if the cell shape changes of LM cells are passive (or non-autonomous).

4.1 Hyperactivation of MyosinII in the entire embryo

It is not clear how the graded MyosinII might affect the apical expansion of LM cells. We wanted to override the MyosinII gradient formation by overexpressing the upstream activating pathway. To observe the effects of overactivation of apical MyosinII, we overexpressed Twist, fog and constitutively active RhoA (RhoV14) in all the cells of the embryo by using a

maternal driver. In embryos overexpressing Twist, fog and RhoV14, a wider furrow was formed and the invagination was. Cells that close the furrow were assumed to be the mesectoderm cells (ME, marked by a blue dot) and were backtraced to define the boundary of the mesodermal cells. The ME cells expand apically and the cells immediately next to them on the ventral direction (red dot) do not expand apically. These neighboring cells are LM cells and they expand in control cells (Fig. 4.1 (a)).

A further detailed analysis is needed to accurately measure apical area changes in embryos activating ectopic apical MyosinII. However, it is indicative from the above preliminary experiments that the LM cells can accumulate apical MyosinII and constrict apically. In control embryos the LM cells do not accumulate apical MyosinII and do not constrict apically. Thus, we think that apical constriction and apical expansion result from different amounts of apical MyosinII.

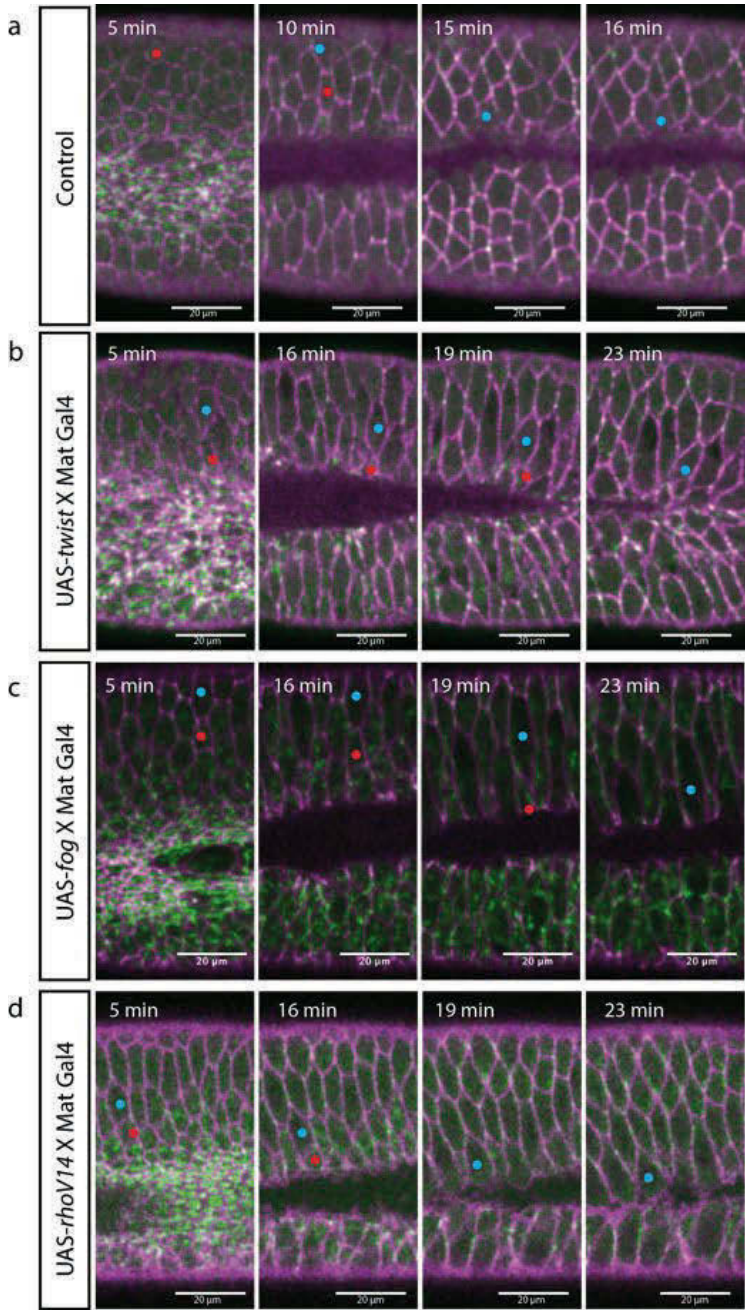

Fig. 4.1 Embryo-wide ectopic activation and recruitment of apical MyosinII. Ventral views of embryos where Twist, Fog and a constitutively active form of Rho1 (RhoV14) are expressed using a maternal driver. Blue dots represent the cells that meet in the middle when the mesoderm is internalized which we assume are the mesectodermal cells (ME). Red dots represent the lateral mesodermal cells that are immediate ventral neighbors of the ME cells. The ME cells (blue dot) in the three experimental conditions expand apically while the LM cells (red dot) constrict apically.

4.2 Controlled inhibition of apical constriction by laser ablation

The experiments done in section 4.1 suggest that the gradient of MyosinII might be important for the apical expansion of the LM. But, using maternal driver, we change the MyosinII distribution in the entire embryo. Thus we needed a method to modify either the MyosinII levels of the effective contractility in a spatially and temporally controlled manner. To test the dependence of LM cell expansion on CM cell apical constriction without affecting levels cellular contractility globally, we used two approaches: a laser based and an optogenetics based approach. In this section I will discribe the first approach where we used a pulsed laser to ablate the apical actomyosin meshwork in the CM cells.

In Fig. 4.2, the embryo was imaged from the ventral side and a pulsed laser was used to ablate the actomyosin meshwork in the region marked by the yellow box. Cyan and red dots mark the LM cells immediately next to the mesectoderm cells in the ablated region (yellow rectangle) and control region respectively. The position of the cells is estimated by observing their positions post-furrow internalization in the non-ablated region.

We observed that the laser causes actomyosin meshwork to break, and repeated exposure to the laser inhibited apical constriction in CM cells. There are cells that do constrict but as an ensemble, the CM cells do not constrict (Fig. 4.2 (a,b)). The control LM cells (red dots) stretch towards the ventral midline and are invaginated. The LM cells adjacent to the laser ablated area (cyan dots) do not stretch, and appear to have reduced apical areas and are not internalized.

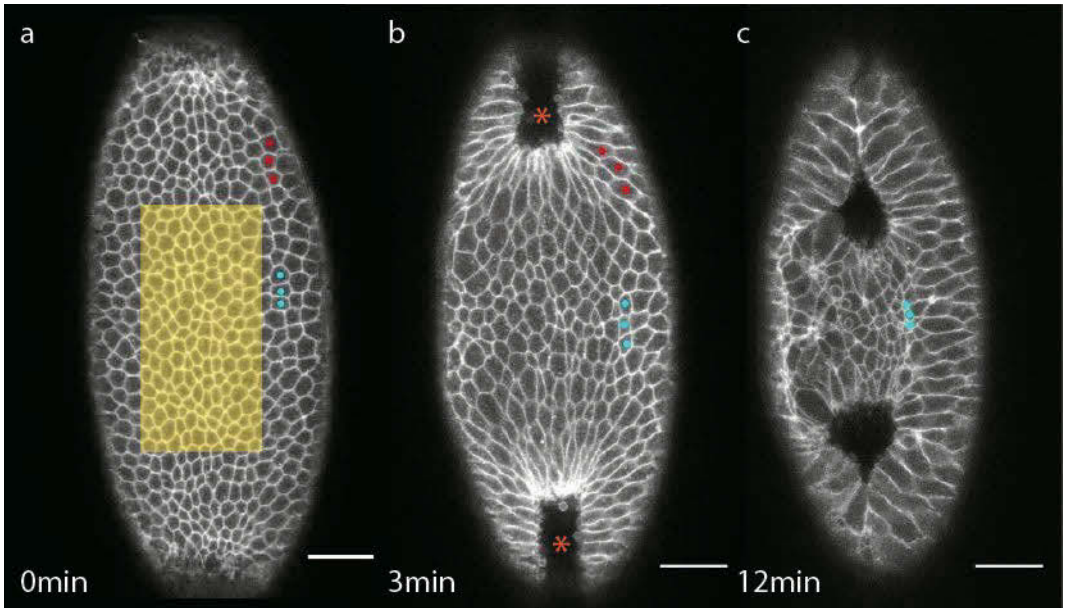

Fig. 4.2 Effect of laser ablation of the apical actomyosin meshwork on apical constriction of CM cells. A region within the CM cells (yellow region) was exposed to pulsed infrared laser on a Z-plane where MyosinII accumulation was observed. (a) The area was exposed every minute for 10 mins and the cells outline marked by GAP43::mCherry were observed. The central-ablated region expands initially (b) but shows mosaic constrictions after 12 min (c). The control non-ablated CM cells constrict and proceed to invagination (orange asterisk). Cells located lateral to the ventral midline and neighboring the control region (red dots), expands and are invaginated. Corresponding cells neighboring the ablated region (cyan dots) do not expand and are not invaginated.

We systematically tested the effect of inhibiting apical constriction of CM cells on apical expansion of the LM cells. To mark the mesoderm boundary, I used the MCP-MS2 system to image *snail* transcription. In control embryos, snail-MS2 transcripts are expressed in all the mesodermal cells but not the ME cells (red; Fig. 4.3 (a-c)). In control embryos, the LM cells (blue) and ME cells expand apically and LM cells are internalised while ME cells meet in the middle to close the furrow. When the apical constriction in CM is inhibited (Fig 4.3 (d-e)) by laser ablation (yellow area) the furrow is not formed and the mesoderm is not invaginated. The LM cells (blue) first expand, then

constrict apically and are not internalised as seen in the control embryos. The ME cells (red) however expand apically(Fig 4.3 (e)).

We conclude that the apical expansion of the LM cells is dependent on apical constriction of the CM cells. The forces generated during apical constriction of CM cells might be necessary for apical expansion of the LM cells.

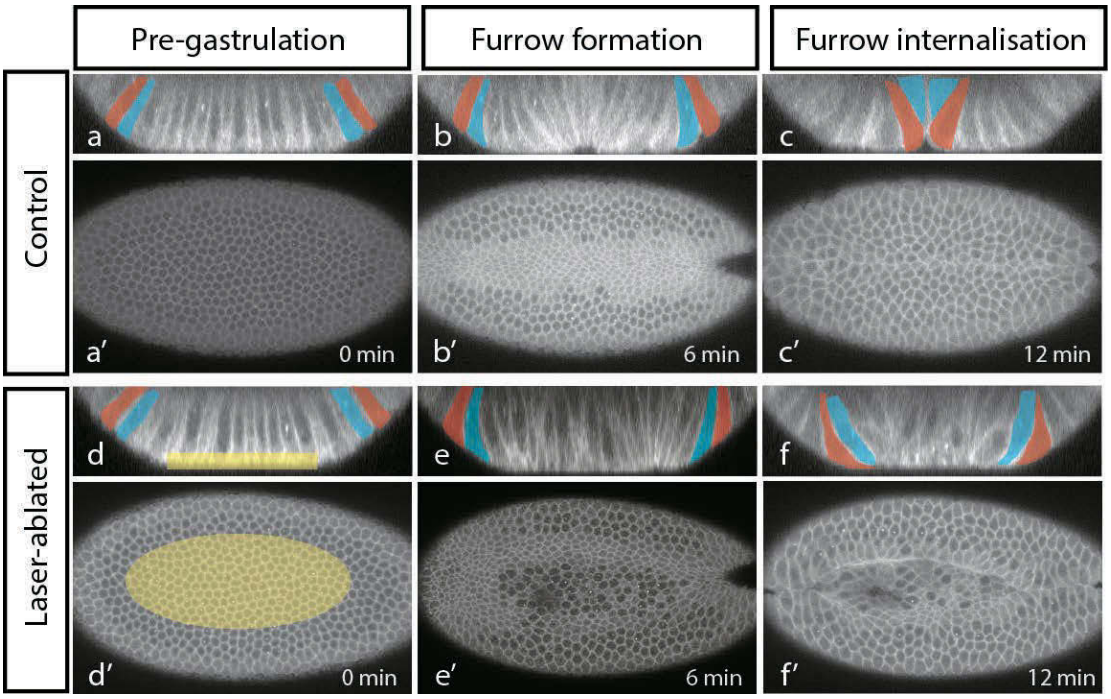

Fig. 4.3 Effect of local inhibition of apical constriction of CM cells on shape changes and movements of the LM cells (blue) and mesectodermal (ME; red) cells. (a,b) In control embryos LM and ME cells expand apically and move towards the ventral midline. (c) LM cells are invaginated while ME cells on the opposite side of the ventral midline fuse to close the furrow. Upon ablation of actomyosin meshwork or CM cells (d,d'; yellow region), the apical constriction is inhibited (e,e'). The LM cells do not expand and move to the same extent as control cells (f). The ME cells are observed to expand apically. The mesodermal cells are marked by visualizing expression of *snail* (white dots) .

4.3 Localised manipulation of cellular contractility using optogenetics

Laser ablation is an efficient way to inhibit apical constriction in a controlled manner, however the laser might have unwanted side effects. To understand the coordination of cell shape changes in the mesodermal cells, we used another approach to inhibit cell contractility locally complementary to the laser ablation experiments. We used optogenetics to reduce cellular contractility in a defined region of interest. The approach is based on dimerization of the Cryptochrome-interacting basic-helix-loop-helix protein (CIB1) with cryptochrome 2 (CRY2) in presence of blue light. The N-terminal domain of CIB1 is tagged with a PM anchor (CIBN-pm) and CRY2 is fused to the catalytic domain of the *Drosophila* inositol polyphosphate 5-phosphatase OCRL, which converts PI(4,5)P2 into phosphatidylinositol-4-phosphate (PI(4)P). PI(4,5)P2 bound actin cortex detaches from PM when CRY2-OCRL is recruited to the PM via CIBN-pm. Thus the effective contractility of the cell is affected[44].

The contractility of the CM cells was reduced optogenetically and shape changes in LM cells were observed. As a marker of the mesoderm boundary, singleminded (sim) expression was visualized using the MCP-MS2 system. Sim is expressed in a single row of ME cells (red cells in Fig. 4.4 d-e). OCRL is recruited to the PM in the blue box (Fig. 4.4 a-b) upon photoactivation. After 10 minutes of repeated photoactivation, a z-stack was taken to observe the 3D shapes of the cells. Fig. 4.4 (d) represents a z-slice 10 microns from the apical surface where the sim expressing ME cells are marked in red and the adjacent LM cells are marked with blue color. The ME cells expand apically but the many of the LM cells (blue) do not expand apically and few are constrict apically. In absence of apical constriction of the CM cells, the LM cells do not expand apically and even constrict apically in some case. However, the ME cells are always observed to expand but the extent of apical expansion might be restricted as the furrow is not internalized

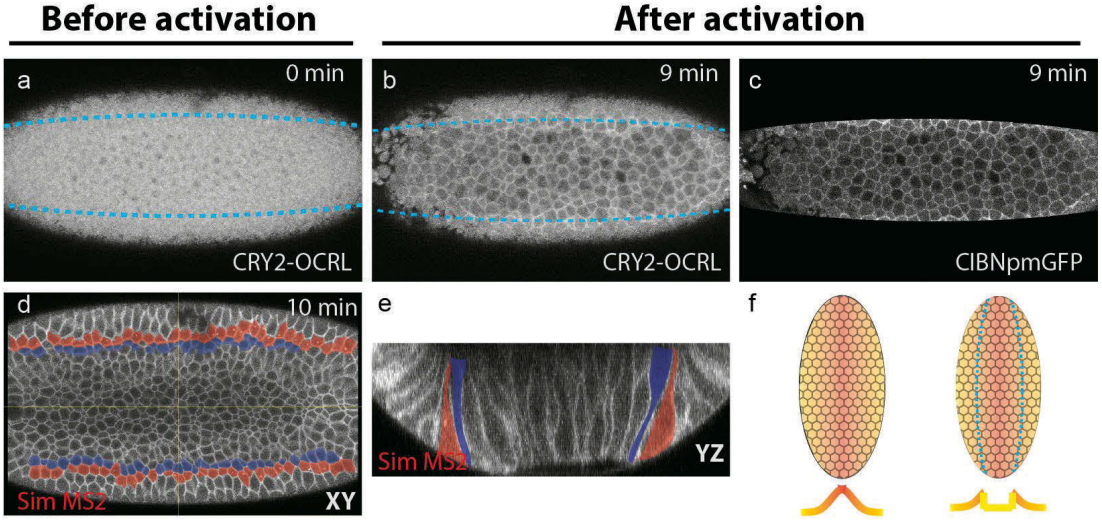

Fig. 4.4 Effect of local inhibition of apical constriction in CM cells on cell shape changes of LM cells. (a) Ventral view of embryo co-expressing CRY2-OCRL and CIBNpmGFP before activation by blue light. (b) Upon activation of CM cells by blue light (region bound by blue dotted line) CRY2-OCRL is recruited to the plasma membrane and apical constriction is inhibited. (c) Apical cross-sectional view visualized by CIBNpmGFP after minutes of repeated activation. (d) Single Z-plane of a stack of the embryo acquired using 2-photon excitation, where mesoderm boundary is marked by expression of *singleminded* (*sim;* red cells). (e)The mesectoderm cells expand apically and the neighboring LM cells constrict apically. (f) A schematic showing the assumed profile of contractility before and after recruitment of OCRL to the plasma membrane.

Localised inhibition of apical constriction using optogenetics shows that the contractile forces generated during apical constriction are necessary for the cell shape in the LM cells. The observation that LM can constrict apically in the above mentioned experimental condition show that LM can constrict when CM cells fail to constrict.

4.4 Localised activation of cellular contractility using optogenetics

The experiments where apical constriction was inhibited by laser ablation and optogenetic OCRL recruitment indicate that there might be a ‘tug-of-war' between the CM and LM cells. We hypothesise that a graded recruitment of apical MyosinII in the mesodermal cells results into a graded contractility of the cells, assuming that amount of MyosinII corresponds directly to the strength of contractility. Thus there is a competition within neighbouring cells of the mesoderm. The LM cells lower amounts of recruit MyosinII than CM cells and cannot counter the contractile force generated by the CM cells. Thus the LM cells deform due to an outcome of a simple force balance.

To test if there is a cellular competition, we used another optogenetic tool to recruit RhoGEF2 apically in the mesodermal cells few rows away from the ventral midline and observed shape changes in all the most ventral mesodermal cells. In these experiments, we used flies expressing the catalytic domain of RhoGEF2 fused to CRY2 (RhoGEF2-CRY2) and the N-terminal domain of CIB1 is tagged with a PM anchor (CIBN-pm). Upon activation by blue light, the catalytic domain of RhoGEF2 is recruited to the PM, where RhoGEF2 promotes recruitment of apical MyosinII[56]. We expect that this ectopic recruitment of apical MyosinII in the lateral cells will counter the contractile forces in the central most cells.

When RhoGEF2 was experimentally recruited to the ventral cells (bound by blue boxes) by photoactivation, the cells near the ventral midline fail to constrict efficiently and did not invaginate. After 12 minutes of activation, a Z-stack was taken to observe the 3D shape changes. In the control region (left side of the embryo in Fig 4.5) the CM cells constrict, LM cells expand and the cells invaginate (Fig. 4.5 (e)). In the region where RhoGEF2 was recruited in lateral cells, the cells near the ventral midline fail to constrict completely and the cells do not invaginate (Fig. 4.5(g)). In the transition region (Fig. 4.5 (f)) the cells do invaginate, but a wide furrow is formed.

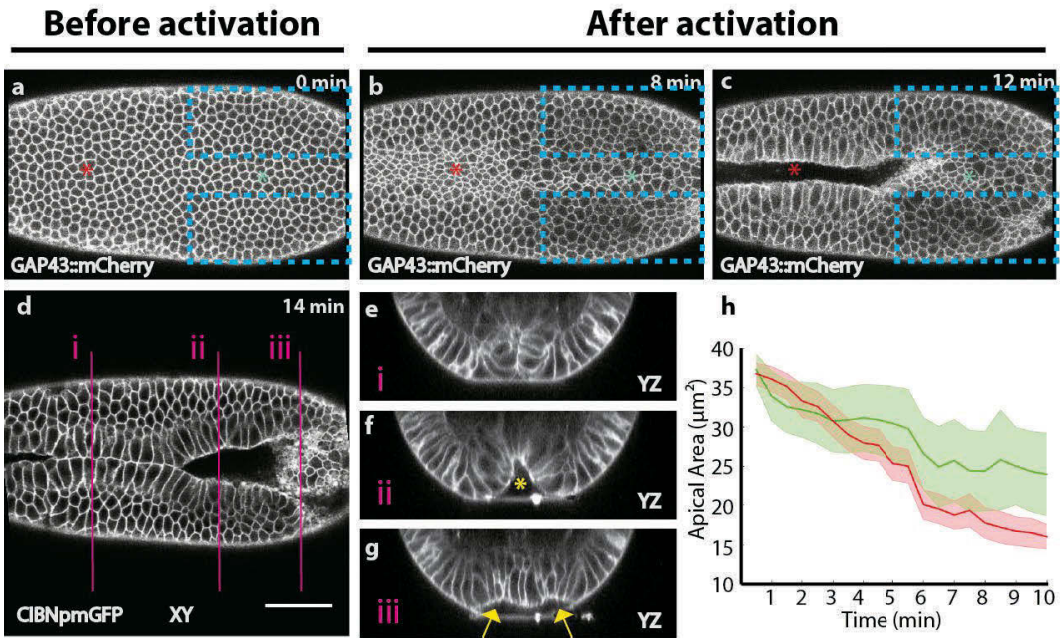

Fig. 4.5 Effect of ectopic activation of apical MyosinII in mesodermal cells on cell shape changes of CM cells. (a) Ventral view of embryo co-expressing CRY2-OCRL and CIBNpmGFP before activation by blue light. (b) Upon activation of CM cells by blue light (region bound by blue dotted line) CRY2-OCRL is recruited to the plasma membrane and apical constriction is inhibited. (c) Apical cross-sectional view visualized by CIBNpmGFP after minutes of repeated activation. (d) Single Z-plane of a stack of the embryo acquired using 2-photon excitation, where mesoderm boundary can be marked by expression of *singleminded*(*sim;* red cells). (e)The mesectoderm cells are observed to expand apically in a YZ cross-section and the neighboring LM cells are observed to constrict apically. (f) A schematic showing profile of contractility before and after recruitment of OCRL to the plasma membrane.

Thus we conclude from the above experiment that there exists a ‘tug-of-war’ within the cells of the mesoderm along the dorsal-ventral axis. The ‘tug-of-war’ however is biased because of the gradient of MyosinII activation across the mesoderm. If the shape of the gradient of the mesoderm is changed, then outcome the cellular ‘tug-of-war’ is changed.

5. Discussion

Improving deep tissue membrane signal detection and segmentation

Imaging and 3D reconstruction of large volumes at high spatial and temporal resolution is a frequent problem in studying live biological samples. Selective plane illumination microscopy (SPIM) has proven to be an effective tool to image large volumes rapidly and with lower phototoxicity than the confocal microscopy. However, SPIM images have low signal to noise ratio which affects the automatic signal detection for segmentation softwares. We can overcome this hurdle by enhancing the signal to noise ratio by processing the raw signal and tailoring imaging and segmentation strategies to the specific problem.

1. We used the high contrast two-photon microscopy images to measure cell volumes of the mesodermal cells. We plotted the cell volumes against the distance of the cell from the ventral midline. The cell volumes are similarly distributed along the ventral-lateral axis. The distribution of the cell volumes does dont change over time indicating the cell volumes of not only the CM but also the LM cells are conserved during the process of ventral furrow formation. It has been proposed that the shape changes at the baso-lateral and basal side of the CM cells is passive and is driven by apical constriction[34]. Similar hypothesis might be true for the LM cells as well. The expansion of apical side of the LM cell might lead to passive deformations in the basolateral and basal sides of the LM cell. We observe a decrease in the basal area of the LM cells. This decrease could be completely passive or might be active constriction via actomyosin meshwork. We did not observe any accumulation of MyosinII near the basal side of the LM cells and thus we think that the basal area decrease might be a passive consequence. It can be a passive consequence of either apical expansion or might be due to the pressure exerted by the nuclei of the LM, which are close to the basal sides of the LM cells.

2. We imaged the ventral half of the embryo with hight temporal resolution to observe the apical area changes using SPIM. The contrast of the membrane signal is not sufficient to resolve basal membranes but is sufficient to observe apical area changes. The apical area measurements were previously done on a single Z-slice[12,25,57]. A single cross sections are representatives of apical area changes when the apical surface is orthogonal to the imaging direction. The approximations of apical areas by cross sections are less accurate for the lateral cells due to the curvature of the embryo. Thus, we extract the apical surface and project them cartographically instead of taking a Z-slice. Thus any errors introduced because of the curvature of the embryo are minimised. Our measurements thus represent the changes in apical area more accurately than the methods before. However, the method is not efficient when the ventral furrow starts to deepen. The method is not sufficient to capture changes in curvatures that have a radius of curvature ~4 fold smaller than the radius of curvature of the embryo.

The measurements reveal an interesting pattern of apical expansion in the LM cells. At the onset of ventral furrow formation the LM cells closest to the ventral midline (VM) expand first and expands the most. These observations suggest that the LM cells do not expand like an elastic sheet of cells. The cells dissipate the forces due to either tissue viscosity or friction with the vitelline membrane. There are a few recent reports suggesting the role of friction between the cells and the vitelline membrane in tissue morphogenesis.

3. Currently SPIM is the only technique capable of imaging the entire embryo. In our study we have imaged entire embryos from multiple angles and used this information to combine into a single 3D image per time point. Thereafter, we have applied a deconvolution algorithm to reduce the blur and improve the contrast of the images. These techniques have been previously applied for imaging and segmenting nuclei signal[58]. Plasma membranes structures are however much narrower as compared to the nuclei and thus the membrane signal is more difficult to image and segment. We have optimized an imaging and processing pipeline for membrane signal large

volume samples that combines multiview imaging and multiview deconvolution methods.

For segmentation of the 3D data, we had earlier applied a marker based watershed algorithm to whole embryo but we failed to get reliable segmentation results for the entire volume of the cells. The results had segmentation errors due to low signal to noise ratio specifically at the basal sides of the cells. So we applied a recently developed pre-processing and segmentation pipeline applied for Arabidopsis tissues[59] and adapted the pipeline for *Drosophila* embryo datasets. In this method, apart from the standard Gaussian noise filtering and corrective morphological gap closing algorithms, we have used convoluted neural networks to enhance membrane signal. We trained a neural network by manual annotations and enhanced the membrane signal where the signal is weak. As we continue to manually annotate more embryos, the neural network is expected to perform better with lower errors. Manual annotation of the data is the most time consuming step, but after having sufficient annotation we expect to have an 'intelligent' neural network that can detect and enhance membrane signal in low contrast images. We expect the consecutive steps of super-voxel generation and merging to perform better with enhanced membrane signal.

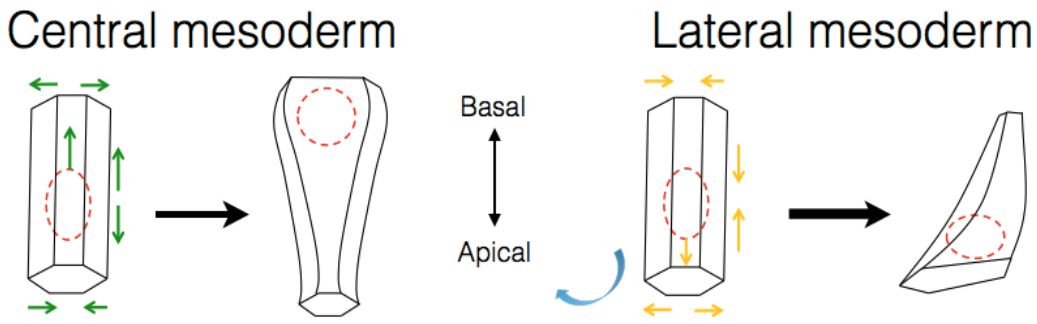

Fig 5.1 Scheme of how the central and lateral mesodermal cells change their shape. In central mesodermal cells, the apical surface constricts, the basal surface relaxes and the cell elongates. In the lateral mesodermal cells, the apical surface expands, the basal surface reduces and the cells shorten.

Gradient of MyosinII activation

A gradient of nuclear Dorsal during nuclear cycle 10-14 provides the positional information to differentiate the Drosophila blastoderm into mesoderm, lateral and dorsal ectoderm. With every nuclear cycle, the width of the nuclear dorsal localisation does not change but the intensity changes. Consequently, *twist,* a Dorsal target gene, is expressed as a bell shaped gradient along the dorsal ventral axis. Observations of anti-Twist stained embryos, reveal that, Twist is expressed in a wider domain of cells (20-24 cell rows) that expands beyond the mesoderm boundary. However, snail expression is restricted by a sharp boundary and snail does not show a graded expression. Expression of the Twist targets, *fog* and *t48* is observed to be in narrower domain (12-14 cell rows) than *twist* expression domain.

Fog and T48 recruit RhoGEF2 in parallel to the apical membrane. Recruitment of RhoGEF2 is necessary and sufficient to recruit and activate MyosinII at the apical side of the cell[56]. Gradient of Fog and T48 is results into a graded recruitment and activation of apical MyosinII. The bell-shape of the apical MyosinII gradient has been hypothesised to be responsible to drive the inward-folding of the mesoderm[12]. The MyosinII gradient leads to a graded distribution of apical areas in the CM cells during furrow formation. But, how the gradient affects the LM cells and how LM cells contribute to furrow formation is not completely understood. We overexpressed Twist using maternal drivers and observed the cell boundaries and MyosinII. By over-expressing *twist*, we expected to override the twist-gradient that is observed in the control embryos. We observe that a wider furrow is formed and cell row ventral to the assumed mesectoderm constricts. We define the mesectoderm as the cells that meet at the middle when the mesoderm is internalised. However, it is known that Twist is required for sustaining expression of snail in the mesoderm[60]. Thus we cannot exclude the possibility that the assumed mesectoderm are patterned differently that in mesectoderm in control embryos.

To override the MyosinII gradient without affecting the nascent twist levels, we overexpressed fog or constitutively active Rho1 (Rho1V14) using a

maternal driver. The overexpression of fog or RhoV14 induces apical accumulation of MyosinII in all cells of the embryo. We observe a wider furrow consistent with previous observation [16,23]. Additionally, the LM cells are observed to constrict. The LM cells are defined by their position, which is next to the cells that touch when mesoderm is internalised. Thus the LM cells are able to constrict as long as there is sufficient activation of RhoGEF2/Rho1 pathway. In gprk2 mutants similar phenotype is observed, the LM cells constrict. A wider furrow is also observed and the mesectoderm are observed to be expanding apically[42]. In all the manipulated conditions listed above, the ventral furrow formation and invagination is significantly delayed. Thus, it is not clear that the LM constrict in these cases because of hyperactivation of MyosinIi or because the apical constriction is delayed.

Pulses in the LM cells

In the central and lateral mesodermal cells , assembly and disassembly cycles of MyosinII coalescence are observed, termed as pulses of MyosinII. When the actomyosin is connected to the plasma membrane , these pulses are accompanied by apical area fluctuations. In the CM cells, initially MyosinII assembles together and is then almost completely disassembled. Onset of ventral furrow formation is marked when these cells do not disassemble MyosinII and start having persistent increase in total MyosinII amount. The persistence or stabilization of medial of MyosinII is thought to cause an irreversible deformation in the PM and lead to a step wise apical constriction. In absence of Twist activity, the CM cells are able to pulse but are reversible, possible because the cells do not have persistent MyosinII levels necessary for irreversible shape change.

In LM cells we observed medial MyosinII pulsing, however there was no accumulation of medial MyosinII. The persistence of medial MyosinII in CM could be due to either stabilization of MyosinII filaments or addition of new MyosinII filament. Lack of accumulation of apical MyosinII in LM cells suggests that LM cells might not be able to stabilize or additionally

recruit medial MyosinII. One of the reasons might be low Twist activity in the LM cells, but this hypothesis needs further testing.

Increased apical area might further hinder stabilization of MyosinII pulses. Cells larger than a certain apical area in cta mutant embryos fail to constrict. These cells are not able to span the entire apical area and cause apical constriction. In the LM cells, the cells have low fog and thus low cta activity. Thus, initial expansion of apical area in LM cells may further lead to destabilisation of the medial MyosinII. We observe 2-3 foci of MyosinII in the expanded LM cells suggesting loss of the radial cell polarity required for apical constriction. Thus there might be direct and indirect effects of an actomyosin gradient across the mesoderm on the actomyosin organisation in the LM cells.

Activators of MyosinII

Active fog and t48 signalling recruit RhoGEF2 apically[14,54]. In the CM cells RhoGEF2 and and its downstream target, Rho1 are previously observed to be localised medially and junctionally in the apical domain[23]. However, the downstream molecule Rock is localised preferentially to only the medial region. Medial localisation of Rock is thought to be due to Twist. How Twist could affect Rock localisation is an open question. In LM cell, there is no accumulation of medial MyosinII and there is a dispersed junctional localisation . To understand what would cause the difference in localisation of MyosinII, we looked at localisation of RhoGEF2 and Rho1 sensor in LM cells. We observe localisation of active Rho1 along the junctions in the LM cells however, there is no localisation of RhoGEF2 along the junctions in the LM cells. This suggests that MyosinII is recruited along the junctions in the LM cells via activation of Rho1 but not via RhoGEF2. There might be another mechanisms that could activate junctional MyosinII in LM.

MyosinII activation in the early embryo is thought to be in a modular fashion[20]. There are some pathways that preferentially activate either medial, junctional or both regions of the cells. GPCR signaling is suggested to be one of the key regulators of MyosinII activation in the early *Drosophila* blastoderm.

Whether such modular behaviour is responsible for differential activation of MyosinII in CM and LM cells is an open question.

Measurement of cortical tension using laser dissection

To test if difference in apical MyosinII recruitment in mesodermal cells might lead to a difference in contractility in CM and LM we performed laser dissections. We assume that the cellular contractility is proportional to the tension across the cell. Measuring recoil velocities after laser dissection has been a widely used method to measure tension in epithelial tissues. Since the contractility is varying along DV axis and not AP axis, we analyzed velocities along only the DV direction. We analyzed the displacements in the first 10 seconds after laser dissection so as to rule out any effects due to cell rearrangement or large scale movements. The recoil velocities of the LM cells is lower than the CM cells suggesting that the LM cells are under lower tension than CM cells. The difference in tension might be a direct consequence of difference in tension.

Manipulating apical constriction using Laser ablation

To locally manipulate cell contractility without affecting the underlying developmental patterning and signalling, we decided to use infrared laser to sever the contractile actomyosin meshwork. Infrared-pulsed laser has been used multiple times to ablate actomyosin meshwork of small population of cells. We tested if the same technique can be used to restrict apical constriction by tuning laser intensities and exposure times. We were able to find proper parameters where we observed that the apical constriction was restricted without any visible damage to the cells. We tested the method of fly lines expressing either GFP of mCherry to the MyosinII and found not difference in effect. Thus we think that the established protocol is different that cytochrome based inactivation of MyosinII.

We ablated a subpopulation of CM cells and observed the effect on the LM cells. We used Snail-MS2 as a marker of mesodermal cells. Laser

ablation delays or halts the apical constriction in laser-illuminated cells and the non-illuminated cells are not affected. When the CM cells do not constrict apically, the LM cells do not expand. Few LM cells are observed to even constrict apically. The mesectodermal (ME) cells are not observed to expand apically. This experiments suggests that LM cells are able to constrict when apical constriction in CM cells is inhibited. Apically constricted LM cells are observed 10-12 mins after onset of apical constriction in the control CM cells. Due to the delayed onset and slow kinetics of apical MyosinII recruitment, the LM cells constrict later. Thus in control conditions, the LM cell have a lower contractility than CM cells and thus expand under the external stretch.

The LM apical constriction observed could possibly be an artifact of the method. Cells are known to recruit MyosinII as a response to calcium influx during wounding. A similar pathway might get upregulated because of actomyosin meshwork ablation or laser illumination. We repeated the laser ablation experiments and did not observe any prominent apical constriction in the neighbourhood of the laser-illuminated region.

Localised manipulation of cellular contractility using optogenetics

To avoid any effects of laser ablation we used and alternative method to inhibit contractility in the CM cell. The method depends on dimerisation of two proteins CRY2 and CIBN (see introduction) upon illumination of blue light. CIBN is anchored to the plasma membrane (PM) and upon activation OCRL fused to CRY2 is recruited to the PM. OCRL severs the connections of actin cortex with the PM. This is an established to reduce contractility of a cell by severing PM connections to the actomyosin meshwork of the CM cells. We inhibited apical constriction in a region covering 8-10 rows of CM cells. We used sim-MS2 as a marker for the mesectoderm cells. Due to limitation of using transgenic construct for a single experiments, we were not able additionally visualise cell boundaries beyond activation region. Thus, we had information of the cell shapes of the LM cells after the experiment had ended.

Due to variability of the maternal driver used in the experiment for expressing CRY2 and CIBN fused constructs, there is wide experimental

variations for this experiments. In extreme cases the actin cortex completely lost connections with PM and the cell lost its shape completely. Analyzing cell any cell shape changes in the LM cells was difficult for such experiment so we choose embryos that showed only moderate effects. In these experiments, the CM cells did not lose ability to constrict apically but apical constriction was incomplete delayed. LM cells were observed to not expand apically and few cells were observed to constrict apically. ME cells were observed to expand apically in these experiments.

The experiments where the apical constriction of CM cells was inhibited using laser ablation or optogenetics, the LM cells failed to expand apically. In few cases the LM cells were also observed to constrict apically. These experiments suggest that the LM cells have the ability to constrict apically, but the kinetics are weaker and slower than in the CM cells. Thus, when the CM cells constrict apically, the external force experienced by the LM cells is larger than its internal contractile force. Thus the apical expansion of the LM cells might be a completely passive cell shape change and is dependent of a tug-of-war induced by gradient of twist.

Localised activation of cellular contractility using optogenetics

To test whether the tug-of-war is sufficient to explain shape changes in mesoderm invagination, we altered the system in a way that the lateral cells have greater contractility than the CM cells. We used the same optogenetic system based on CRY2 and CIBN, but we used CRY2 fused with the catalytic domain of RhoGEF2. Thus when RhoGEF2 is recruited by activation of blue light, MyosinII gets recruited. This method has been shown recently to cause controlled ectopic apical constriction. We used this to induce apical constriction a subset of cells on either side of the VM. We observed the cell shape changes in the part in between the activated regions. Inducing apical constriction in the lateral cells inhibited the apical constriction. This suggests that a tug-of-war might be one of the reasons why the ventral most cells constrict first and stronger than its lateral neighbors.

Concluding remarks

Cell shape changes are a consequence of forces generated within the cell (autonomous forces) and forces exerted by its environment (non autonomous). In tissues, individual cell shape change depends on the autonomous forces generated by the cell and non-autonomous forces exerted by the neighbours and the extracellular matrix. In a broader context, the autonomous force generating cells and passive responding cells due to non-autonomous forces determines tissue shape.

Conceptually, it is easier to understand a tissue-wide force balance when force generating cells and passive responding cells are separated by a sharp border (illustrated in the Fig4.1). This border can be result of developmental patterning in some case. In *Drosophila* blastoderm, the autonomous forces generated by the central mesodermal cells (CM), drive the formation and internalisation of the mesoderm. The lateral mesodermal cells (LM) expand apically and tuck in the CM cells, while the ectodermal cells

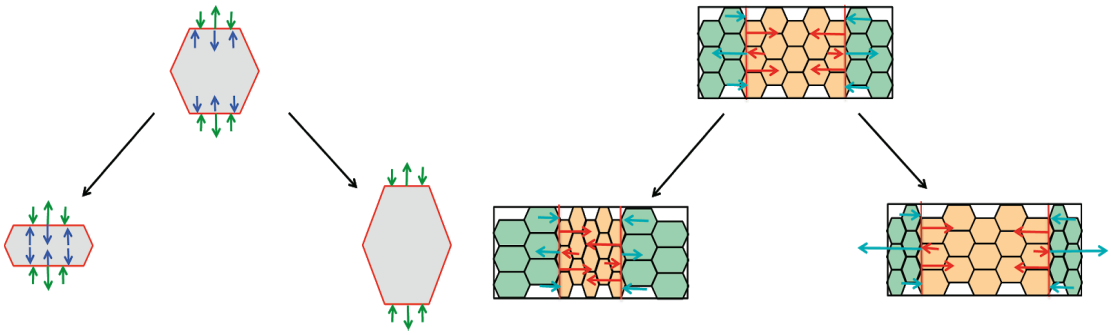

Fig. 5.2 Schematic of how force balance results to cell or tissue level deformation. Arrow in the figure represents forces acting on the cell and the tissue. The direction of the arrow corresponds to the direction of the force.

retain their shape and move as a cohort ventrally. A sharp boundary between mesodermal and ectodermal cells defined by snail *expression* can explain the difference in cell behaviours of the ectodermal cells. However, scenario within the mesoderm is more complicated. There is no clear genetic boundary, yet a virtual boundary is created between the CM and LM cells.

In this thesis we present mechanisms of how cells deform non-autonomously and how cell shapes are coordinated during ventral furrow formation in *Drosophila* embryo. We find that a graded activation of MyosinII induces a cellular ‘tug-of-war’ across the mesodermal cells. Cells closest to the VM generate contractile forces stronger than the lateral cells and causes the LM cells to expand their apical surface. When the lateral mesodermal cells do not expand, a wider furrow is observed and furrow internalisation is delayed. We think that the permissive apical expansion of lateral mesoderm cells facilitates rapid invagination of the mesoderm.

In the thesis I have studied the interaction between the LM and CM cells. In future I would like to understand how the cell shapes are coordinated in 3D in the entire embryo. We have established imaging and segmentation tools to extract in principle the cell shapes of all the cells of the embryo. With improved tracking of individual cells we will be able to have a detailed understanding of the individual cell shape changes during gastrulation.

6. Material and methods

Fly stocks and crosses

All the flies were maintained at 25 degree C using all standard practices. Following fly stocks were used in this study :

Table 1. List of fly stocks

Stock	Stock information
w[*]; p[UASp-GAP43:: Venus]; +	Bloomington stock 30896
w[*]; p[UAS-sqh-Gap43::mCherry]/CyO; +	Gift from Thomas Lecuit (GAP43-mCherry;Martin et al 2010 [26])
w[*]; p[sqh-MRLC::eGFP]/Cyo; p[UASp-Gap43::mCherry]/MKRS	Gift from Thomas Lecuit (sqh-GFP; Royou et al., 2002)
sqh^{AX3};p[sqh-UtrophinABD::GFP], p[sqh-MRLC::mCherry]	Gift from Thomas Lecuit (sqh-mCherry; Martin et al., 2009)
sqh^{AX3}; p[sqh-MRLC::mCherry]; p[Spider::GFP]	Gift from Stefano DeRenzis (Martin et al 2010)
w[*]; p[ubi-anilinRBD::GFP], p[sqh-MRLC::mCherry]	Gift from Thomas Lecuit [20]
w[*]; p[UASp-sqh-GAP43::mCherry]; RhoGEF2::GFP	Gift from Thomas Lecuit (RhoGEF2-GFP;Mason et al 2016 [23])
w[*]; p[UASp-twist]/p[UAS-twist]; +	Leptin lab
w[*]; + ; p[UASp-fog]/TM6,Tb,Hu	Gift from Thomas Lecuit

w[*]; p[UASp-RhoV14]/CyO	Bloomington stock 7333
w[*]; P[w+,matαTub-Gal4::VP16]; p[sqh-MRLC::mCherry], p[endoCAD::GFP]	Gift from Thomas Lecuit (Munjal et al 2015[32])
w[*]; p[snail::MS2]; +	Gift from Jacques Bothma (Bothma et al 2015[10])
w[*]; p[MCP::mCherry]/CyO ; p[MCP::mCherry]/TM3,Ser	Gift from Jacques Bothma(Bothma et al 2018[61])
w[*]; + ; P[w+,UASp-mCherry::CRY2-OCRL]/ Sb	Gift from Stefano DeRenzis (Guglielmi et al 2015[44])
w[*]; P[w+,UASp-CIBN::pmGFP]//Cyo ; sb/TM3,Sb	Gift from Stefano DeRenzis (Guglielmi et al 2015[44])
w[*]; p[MCP::GFP]	Gift from Stefano DeRenzis (Garcia et al 2013[62])
w[*]; p[Sim::MS2]	Gift from Stefano DeRenzis
w[*]; p[UASp-RhoGEF2-CRY2]/TM3, Ser	Gift from Stefano DeRenzis(Izquierdo et al 2018[56])
p[sqh::GFP];p[w+,matαTub-Gal4::VP16],p[UASp-Gap43::mCherry::mCherry]/TM3	Gift from Adam Martin (Vasquez et al 2014[63])
w[*]; If/CyO; p[Oskp-Gal4::VP16]/TM3, Ser	Bloomington stock 23651
p[sqhp-Gap43::mCherry]; +; +	Gift from Stefano DeRenzis (Izquierdo et al 2018[56])

Table 2. List of genotypes of embryos and crosses used in experiments

Figure no.	Fly stock/ Cross
2.1	w[*]; p[UASp-GAP43:: Venus]; +
2.2, 2.3, 2.4 2.5, 2.7, 2.8	w[*]; p[UASp-sqh-Gap43::mCherry]/CyO
3.1, 4.2	p[sqh-MRLC::GFP/Cyo]; p[UASp-sqh-Gap43::mCherry]/MKRS
3.2, 3.5	sqh^{AX3}; p[sqh-UtrophinABD::GFP], p[sqh-MRLC::mCherry]
3.3	sqh^{AX3}; p[sqh-sqh::mCherry]; p[Spider::GFP]
3.4 a-f, a'-f'	p[ubi-AnilinRBD::GFP], p[sqh-MRLC::mCherry]
3.4 g-i, g'-i'	p[UASp-sqh-GAP43::mCherry]; GFP::RhoGEF2
4.1 a	p[sqh-sqh::GFP]; p[w+,matαTub-Gal4::VP16], p[UASp-sqh-GAP43::mCherry]/TM3
4.1 b	p[w+,matαTub-Gal4::VP16]/+; p[sqh-MRLC::mCherry], p[endoCAD::GFP]/p[UAS-fog]
4.1 c	p[w+,matαTub-Gal4::VP16]/p[UAS-twist]; p[sqh-MRLC::mCherry], p[endoCAD::GFP]/+
4.1 d	p[sqh-sqh::GFP]/p[UASp-RhoV14]; p[w+,matαTub-Gal4::VP16],p[UASp-sqh-Gap43::mCherry]/+
4.3	p[sqh-MRLC::eGFP]/p[MCP::mCherry];p[UASp-sqh-Gap43::mCherry]/p[MCP::mCherry] X p[Snail::MS2]/p[Snail::MS2]
4.4	p[UASp-CIBN::pmGFP]/p[MCP::GFP]; p[UAS-OCRL-CRY2::mCherry]/p[Osk-Gal4::VP16] X p[Sim::MS2]/p[Sim::MS2]
4.5	p[sqhp-Gap43::mCherry]/+; p[UASp-CIBN::pmGFP] ; p[UASp-RhoGEF2-CRY2] / p[Osk-Gal4::VP16]

Materials

Material used in the study are listed in the following table :

Table 3. Materials

Product name	Product information
Glass bottom plates	Matek corporation (Part no.: P35G-1.5-10.C)
Microspheres	TetraSpeck™ Fluorescent Microspheres, ThermoFisher (Catalogue no.:T7284)
Gelrite	Merck (Catalogue no.:G1910)
Halocarbon Oil 27	Merck (Catalogue no.:H8773)

Confocal microscopy

Embryos were collected on an apple juice agar plate from a standard cages containing the adults. Plates were changed after one hour embryo collection and were kept at 25 degree C for two and half hours. Mid to late cellularization embryos were selected using halocarbon 27 oil. The stage selected embryos were devittelanised using 50% bleach and washed thoroughly with distilled water. The embryos were then mounted on a glass bottom microwell dish with ventral side facing the glass. The embryos were then covered with 1XPBS.

For visualising cell shapes using 2-photon illumination, femtosecond-pulsed infrared laser (Chameleon Compact OPO Family, Coherent) tuned at 950 nm emission wavelength and coupled with Zeiss LSM 780 confocal microscope was used. The Zen 'Regions' interface was used to create the region of interest and the embryos were illuminated with 10-15% laser power. A volume of 200 x 500 x 60 μm^3 (Height X Width X Depth) at the middle of embryo from the anterior-posterior axis was imaged.

For observing F-actin, MyosinII, RhoGEF2 and AnilinRBD, C-Apochromat 63X magnification oil immersion Zeiss Objective with 1.4 NA was

used. Image stacks were acquired with a Z-spacing of 0.5 µm and a maximum intensity Z- projections of the 2µm from the apical surface was used to visualise the apical signal.

Laser ablation and illumination

Laser-based actomyosin meshwork ablation was performed using a femtosecond-pulsed infrared laser (Chameleon Compact OPO Family, Coherent) tuned at 950 nm emission wavelength and coupled with LSM Zeiss 780 confocal microscope. The Zen Bleaching interface was used to create the region of interest and was illuminated at 65-70% laser power. For this experiment, C-Apochromat 63X magnification water immersion Zeiss Objective with 1.1 NA was used (infrared corrected).

For measuring initial recoil velocities after laser dissection, Particle Image Velocimetry was performed using PIVlab software (MatLab). For first step, 64 x 64 and for second step, 32 x 32 pixels query window was used. The velocities between +-3µm/sec were considered for all frames. Distance Vs time plots were generated using the average velocities in every time frame multiplied by time per frame. Linear fit was applied to the data of first 10-15 frames and value of initial velocity was determined from the slope of the linear fit.

Optogenetic manipulations

For imaging the optogenetic constructs, all the crosses were kept in dark. Screening of intermediate crosses were done in a dark room and filters were used to filter out any blue light. Dimerisation of CRY2 and CIBN proteins was facilitated by using an infrared laser (Chameleon Compact OPO Family, Coherent) tuned to 950 nm emission. The males and females expressing CRY2 and CIBN fusion proteins were caged at 25□ in dark (inside a cardboard box). The embryos were collected on an apple juice agar plates and mid-cellularising embryos were selected using Halocarbon Oil 27 (Sigma aldrich). Embryos were mounted ventrally on a glass-bottom plate. The Zen ‘Regions’ interface was used to create the region of interest and the embryos

were illuminated with 15-20% laser power. For this experiment, C-Apochromat 40X magnification water immersion Zeiss Objective with 1.2 NA was used (infrared corrected).

Selective plane illumination microscopy and image processing

Embryos were collected on an apple juice agar plate from a standard cages containing the adults. Plates were changed after one hour embryo collection and were kept at 25 degree C for two and half hours. Mid to late cellularization embryos were selected using halocarbon 27 oil. The stage selected embryos were devittelanised using 50% bleach and washed thoroughly with distilled water. Embryos were mounted in 1% Gelrite inside a glass capillary.

Image acquisition: Imaging was performed using a LuXendo MuVi-SPIM. Illumination was done using Nikon 10/0.3W objective lenses and detection with Nikon 20/1.0W objective lenses. An additional 1.5X magnification tube lens was used resulting in an effective image pixel size of 0.19 µm X 0.19 µm. Optical sections of an embryo were recorded with a typical spacing of 0.75-1 µm. For visualising MyosinII (FigX) *sqh-MRLC::GFP ;GAP43::mCherry* embryos were imaged from two opposing directions simultaneously and successively from two directions normal to the first two. For observing cell shape changes, *GAP43::mCherry* embryos were imaged from two opposing directions simultaneously and successively from three directions with 60 degree apart. The embryos were imaged while embedded in 0.5µm spheres (beads) or additional beads were recorded to enable bead based registration.

Pre-processing: The acquired images contain a certain percentage of randomly distributed ‘dead pixels’. These dead pixels are represented by zero intensity value. To avoid any further processing errors, the images are corrected by replacing the dead pixels with an average intensity value of the neighbouring pixels.

MultiView registration: Four or Six image stacks per time point were fused into one isotropic image using BigStitcher Fiji plugin. This involves initial coarse manual registration followed by a bead based registration and image based refined registration.

First, the images were imported in the BigStitcher software. We used only the first time point to determine the coarse registration parameters. All the view were rotated to correct for the rotation used while image acquisition. Then, 'Bead based registration' was performed using the beads embedded in the mounting gel or were recorded separately. These coarse registration parameters were propagated through the entire time series. For refined registration ' image-landmark based registration' module was used. In this process, image landmarks (tri cellular junctions and intensity minima at the centers of the cells) were used to determine refined registration parameters.

Multiview deconvolution: The Point spread function (PSF) for the MuVi SPIM are predetermined using sub-resolution (200 nm) microspheres. These PSFs are distorted from an ideal 3D gaussian intensity distribution which represent the distortion due to the optical system of the microscope. This systematic distortion can be corrected using deconvolution algorithms from the BigStitcher software. We used *Efficient Bayesian Optimisation* iteration and the deconvolved image was produced after 15 iterations.

Apical surface extraction from SPIM images

A 50 pixel radius Gaussian filtering and thresholding was used to extract the shape of the embryo. Using the high contrast between the blurred embryo and background, the image was distance transformed. In a distance transformed image, intensity of each pixel is proportional to the distance from the surface of the embryos. By using intensity thresholding, we can select two-three pixel wide "peel" on the surface of the embryo. The thresholded image is converted to a binary image mask. The apical surface of the embryos is then extracted by applying the binary mask to the raw (input) image.

Image analysis and data visualisation

Image operation like cropping, z-projecting and taking the transverse sections were performed using Fiji[48]. All the graphs were plotted using either Matlab (Matlab_R2015a) or Python(version 3.6). The figures were compiled using Adobe Illustrator CS6 (Version 16.0.0).

To generate the plots in the Fig. 2.6 and Fig. 2.7, either volume or apical area for every cell was plotted first. Then the cells were divided in to bins, depending upton their distances from the ventral midline (Bin size= 10 micrometers). Mean was calculated for every all the cells in a bin and was plotted as a function of the distance from the ventral midline.

Acknowledgements

The work presented in the thesis has been carried out in the lab of Maria Leptin at the European Molecular Biology Laboratory (EMBL), Heidelberg. I am grateful to Maria for giving me the opportunity to work with her group. I thank Maria, the current and past lab members for the exciting discussions and for the critical remarks. I specially thank Daniel, Matteo and Paola for helping me to develop research skills in the first years of the PhD. I thank my thesis committee members Lars Hufnagel, Takashi Hiiragi and Steffen Lemke for their support and suggestion on the project.

I thank Lars Hufnagel and his group for introducing me to SPIM imaging. I specially thank Gustavo Quintas Glasner de Medeiros and Dimitri Kromm for helping and teaching me details of SPIM imaging. I thank Tobias Rasse for guiding me through the SPIM-image processing protocols. I thank Johannes Stegmaier for the collaborative work on SPIM image processing and image segmentation. I thank the members of Advanced Light microscopy facility (ALMF) at EMBL for the training and technical support for the confocal microscopy.

Last but not the least, I thank my family and friends for supporting me throughout this rollercoaster ride called ‘PhD’.

Bibliography

1 Leptin, M. & B., G. Cell shape changes during gastrulation in *Drosophila*. *Development* (1990).

2 Sweeton, D., Parks S., Costa, M. & Wieschaus, E. Gastrulation in Drosophila- the formation of the ventral furrow and posterior midgut invaginations. (1991).

3 Woolner, S. Morphogenesis: joining the dots to shape an embryo. *Curr Biol* **17**, R289-291, doi:10.1016/j.cub.2007.02.016 (2007).

4 Rauzi, M. *et al.* Embryo-scale tissue mechanics during Drosophila gastrulation movements. *Nat Commun* **6**, 8677, doi:10.1038/ncomms9677 (2015).

5 D. Morisato, K. V. A. Signaling Pathways that Establish the Dorsal-Ventral Pattern of the Drosophila Embryo. *Annual reviews of Genetics* (1995).

6 Rushlow , H., Manley and Levine. The Graded Distribution of the *dorsal* Morphogen is initiated by selective nuclear transport in *Drosophila*. *Cell* (1989).

7 Roth, D. S., Christiane Nüsslein-Volhard. A gradient of nuclear localization of the dorsal protein determines dorsoventral pattern in the Drosophila embryo. (1989).

8 Simpson, P. Maternal-Zygotic Gene Interactions during Formation of the Dorsoventral Pattern in Drosophila Embryos. *Genetics* **105**, 615-632 (1983).

9 Grau, Y., Carteret, C. & Simpson, P. Mutations and Chromosomal Rearrangements Affecting the Expression of Snail, a Gene Involved in Embryonic Patterning in Drosophila Melanogaster. *Genetics* **108**, 347-360 (1984).

10 Bothma, J. P. *et al.* Enhancer additivity and non-additivity are determined by enhancer strength in the Drosophila embryo. *Elife* **4**, doi:10.7554/eLife.07956 (2015).

11 Kam, Z., Minden, J. S., Agard, D. A., Sedat, J. W. & Leptin, M. Drosophila gastrulation: analysis of cell shape changes in living embryos by three-dimensional fluorescence microscopy. *Development* **112**, 365-370 (1991).

12 Heer, N. C. *et al.* Actomyosin-based tissue folding requires a multicellular myosin gradient. *Development* **144**, 1876-1886, doi:10.1242/dev.146761 (2017).

13 Morel, V. & Schweisguth, F. Repression by suppressor of hairless and activation by Notch are required to define a single row of single-minded expressing cells in the Drosophila embryo. *Genes Dev* **14**, 377-388 (2000).

14 Kolsch, V., Seher, T., Fernandez-Ballester, G. J., Serrano, L. & Leptin, M. Control of Drosophila gastrulation by apical localization of adherens junctions and RhoGEF2. *Science* **315**, 384-386, doi:10.1126/science.1134833 (2007).

15 Costa, M., Wilson, E. T. & Wieschaus, E. A putative cell signal encoded by the folded gastrulation gene coordinates cell shape changes during Drosophila gastrulation. *Cell* **76**, 1075-1089 (1994).

16 Morize, P. & Audrey E. Christiansen, M. C., Suki Parks and Eric Wieschaus. Hyperactivation of the folded gastrulation pathway induces specific cell shape changes. *Development* (1998).
17 Lim, B., Levine, M. & Yamazaki, Y. Transcriptional Pre-patterning of Drosophila Gastrulation. *Curr Biol* **27**, 286-290, doi:10.1016/j.cub.2016.11.047 (2017).
18 Dawes-Hoang, R. E. *et al.* folded gastrulation, cell shape change and the control of myosin localization. *Development* **132**, 4165-4178, doi:10.1242/dev.01938 (2005).
19 Manning, A. J., Peters, K. A., Peifer, M. & Rogers, S. L. Regulation of epithelial morphogenesis by the G protein-coupled receptor mist and its ligand fog. *Sci Signal* **6**, ra98, doi:10.1126/scisignal.2004427 (2013).
20 Kerridge, S. *et al.* Modular activation of Rho1 by GPCR signalling imparts polarized myosin II activation during morphogenesis. *Nat Cell Biol* **18**, 261-270, doi:10.1038/ncb3302 (2016).
21 Parks, S. & Wieschaus, E. The Drosophila gastrulation gene concertina encodes a G alpha-like protein. *Cell* **64**, 447-458 (1991).
22 Mathew, S. J., Rembold, M. & Leptin, M. Role for Traf4 in polarizing adherens junctions as a prerequisite for efficient cell shape changes. *Mol Cell Biol* **31**, 4978-4993, doi:10.1128/MCB.05542-11 (2011).
23 Mason, F. M., Xie, S., Vasquez, C. G., Tworoger, M. & Martin, A. C. RhoA GTPase inhibition organizes contraction during epithelial morphogenesis. *J Cell Biol* **214**, 603-617, doi:10.1083/jcb.201603077 (2016).
24 Perez-Mockus, G. *et al.* Spatial regulation of contractility by Neuralized and Bearded during furrow invagination in Drosophila. *Nat Commun* **8**, 1594, doi:10.1038/s41467-017-01482-8 (2017).
25 Martin, A. C., Kaschube, M. & Wieschaus, E. F. Pulsed contractions of an actin-myosin network drive apical constriction. *Nature* **457**, 495-499, doi:10.1038/nature07522 (2009).
26 Martin, A. C., Gelbart, M., Fernandez-Gonzalez, R., Kaschube, M. & Wieschaus, E. F. Integration of contractile forces during tissue invagination. *J Cell Biol* **188**, 735-749, doi:10.1083/jcb.200910099 (2010).
27 Levayer, R. & Lecuit, T. Biomechanical regulation of contractility: spatial control and dynamics. *Trends Cell Biol* **22**, 61-81, doi:10.1016/j.tcb.2011.10.001 (2012).
28 Koenderink, G. H. & Paluch, E. K. Architecture shapes contractility in actomyosin networks. *Curr Opin Cell Biol* **50**, 79-85, doi:10.1016/j.ceb.2018.01.015 (2018).
29 Belmonte, J. M., Leptin, M. & Nedelec, F. A theory that predicts behaviors of disordered cytoskeletal networks. *Mol Syst Biol* **13**, 941, doi:10.15252/msb.20177796 (2017).
30 Wollrab, V., Julio M Belmonte, Maria Leptin, Francois Nedelec & Koenderink, G. H. Polarity sorting drives remodeling of actin-myosin networks. *BiorXiv* (2018).
31 Coravos, J. S., Mason, F. M. & Martin, A. C. Actomyosin Pulsing in Tissue Integrity Maintenance during Morphogenesis. *Trends Cell Biol* **27**, 276-283, doi:10.1016/j.tcb.2016.11.008 (2017).

32 Munjal, A., Philippe, J. M., Munro, E. & Lecuit, T. A self-organized biomechanical network drives shape changes during tissue morphogenesis. *Nature* **524**, 351-355, doi:10.1038/nature14603 (2015).
33 Clement, R., Dehapiot, B., Collinet, C., Lecuit, T. & Lenne, P. F. Viscoelastic Dissipation Stabilizes Cell Shape Changes during Tissue Morphogenesis. *Curr Biol* **27**, 3132-3142 e3134, doi:10.1016/j.cub.2017.09.005 (2017).
34 Gelbart Michael *et al.* Volume conservation priciple involved in cell lenghening and nucleus movement during tissue morphogenesis. *Proc Natl Acad Sci U S A* (2012).
35 Harris, T. J. & Peifer, M. Adherens junction-dependent and -independent steps in the establishment of epithelial cell polarity in Drosophila. *J Cell Biol* **167**, 135-147, doi:10.1083/jcb.200406024 (2004).
36 Harris, T. J. Adherens junction assembly and function in the Drosophila embryo. *Int Rev Cell Mol Biol* **293**, 45-83, doi:10.1016/B978-0-12-394304-0.00007-5 (2012).
37 Schejter, E. D. & Wieschaus, E. bottleneck acts as a regulator of the microfilament network governing cellularization of the Drosophila embryo. *Cell* **75**, 373-385 (1993).
38 Weng, M. & Wieschaus, E. Myosin-dependent remodeling of adherens junctions protects junctions from Snail-dependent disassembly. *J Cell Biol* **212**, 219-229, doi:10.1083/jcb.201508056 (2016).
39 Weng, M. & Wieschaus, E. Polarity protein Par3/Bazooka follows myosin-dependent junction repositioning. *Dev Biol* **422**, 125-134, doi:10.1016/j.ydbio.2017.01.001 (2017).
40 Cavey, M., Rauzi, M., Lenne, P. F. & Lecuit, T. A two-tiered mechanism for stabilization and immobilization of E-cadherin. *Nature* **453**, 751-756, doi:10.1038/nature06953 (2008).
41 Xie, S. & Martin, A. C. Intracellular signalling and intercellular coupling coordinate heterogeneous contractile events to facilitate tissue folding. *Nat Commun* **6**, 7161, doi:10.1038/ncomms8161 (2015).
42 Fuse, N., Yu, F. & Hirose, S. Gprk2 adjusts Fog signaling to organize cell movements in Drosophila gastrulation. *Development* **140**, 4246-4255, doi:10.1242/dev.093625 (2013).
43 Chanet, S. *et al.* Actomyosin meshwork mechanosensing enables tissue shape to orient cell force. *Nat Commun* **8**, 15014, doi:10.1038/ncomms15014 (2017).
44 Guglielmi, G., Barry, J. D., Huber, W. & De Renzis, S. An Optogenetic Method to Modulate Cell Contractility during Tissue Morphogenesis. *Dev Cell* **35**, 646-660, doi:10.1016/j.devcel.2015.10.020 (2015).
45 Sun, Z. *et al.* Basolateral protrusion and apical contraction cooperatively drive Drosophila germ-band extension. *Nat Cell Biol* **19**, 375-383, doi:10.1038/ncb3497 (2017).
46 Hörl, D. *et al.* BigStitcher: Reconstructing high-resolution image datasets of cleared and expanded samples. *bioRxiv* (2018).
47 Preibisch, S. *et al.* Efficient Bayesian-based multiview deconvolution. *Nat Methods* **11**, 645-648, doi:10.1038/nmeth.2929 (2014).
48 Schindelin, J. *et al.* Fiji: an open-source platform for biological-image analysis. *Nat Methods* **9**, 676-682, doi:10.1038/nmeth.2019 (2012).

49 Khan, Z., Wang, Y. C., Wieschaus, E. F. & Kaschube, M. Quantitative 4D analyses of epithelial folding during Drosophila gastrulation. *Development* **141**, 2895-2900, doi:10.1242/dev.107730 (2014).
50 Field, C. M., Coughlin, M., Doberstein, S., Marty, T. & Sullivan, W. Characterization of anillin mutants reveals essential roles in septin localization and plasma membrane integrity. *Development* **132**, 2849-2860, doi:10.1242/dev.01843 (2005).
51 Fox, D. T. & Peifer, M. Abelson kinase (Abl) and RhoGEF2 regulate actin organization during cell constriction in Drosophila. *Development* **134**, 567-578, doi:10.1242/dev.02748 (2007).
52 Maitre, J. L. *et al.* Adhesion functions in cell sorting by mechanically coupling the cortices of adhering cells. *Science* **338**, 253-256, doi:10.1126/science.1225399 (2012).
53 Winklbauer, R. Cell adhesion strength from cortical tension - an integration of concepts. *J Cell Sci* **128**, 3687-3693, doi:10.1242/jcs.174623 (2015).
54 Barrett, K., Leptin, M. & Settleman, J. The Rho GTPase and a putative RhoGEF mediate a signaling pathway for the cell shape changes in Drosophila gastrulation. *Cell* **91**, 905-915 (1997).
55 Conte, V. *et al.* A biomechanical analysis of ventral furrow formation in the Drosophila melanogaster embryo. *PLoS One* **7**, e34473, doi:10.1371/journal.pone.0034473 (2012).
56 Izquierdo, E., Quinkler, T. & De Renzis, S. Guided morphogenesis through optogenetic activation of Rho signalling during early Drosophila embryogenesis. *Nat Commun* **9**, 2366, doi:10.1038/s41467-018-04754-z (2018).
57 Spahn, P. & Reuter, R. A Vertex Model of Drosophila Ventral Furrow Formation. *PLoS ONE* **8**, e75051, doi:10.1371/journal.pone.0075051 (2013).
58 Krzic, U., Gunther, S., Saunders, T. E., Streichan, S. J. & Hufnagel, L. Multiview light-sheet microscope for rapid in toto imaging. *Nat Methods* **9**, 730-733, doi:10.1038/nmeth.2064 (2012).
59 Johannes Stegmaier *et al.* Cell Segmenation in 3D Confocal images using Supervoxel Merge-Forests with CNN-based Hypothesis selection. *arXiv* (2017).
60 Ip, Y. T., Park, R. E., Kosman, D., Yazdanbakhsh, K. & Levine, M. dorsal-twist interactions establish snail expression in the presumptive mesoderm of the Drosophila embryo. *Genes Dev* **6**, 1518-1530 (1992).
61 Bothma, J. P., Norstad, M. R., Alamos, S. & Garcia, H. G. LlamaTags: A Versatile Tool to Image Transcription Factor Dynamics in Live Embryos. *Cell* **173**, 1810-1822 e1816, doi:10.1016/j.cell.2018.03.069 (2018).
62 Garcia, H. G., Tikhonov, M., Lin, A. & Gregor, T. Quantitative imaging of transcription in living Drosophila embryos links polymerase activity to patterning. *Curr Biol* **23**, 2140-2145, doi:10.1016/j.cub.2013.08.054 (2013).
63 Vasquez, C. G., Tworoger, M. & Martin, A. C. Dynamic myosin phosphorylation regulates contractile pulses and tissue integrity during epithelial morphogenesis. *J Cell Biol* **206**, 435-450, doi:10.1083/jcb.201402004 (2014).